

Volcanic trigger of ocean deoxygenation during Cordilleran ice sheet retreat

Journal Article

Author(s):

Du, Jianghui ; Mix, Alan C.; Haley, Brian A.; Belanger, Christina L.; Sharon

Publication date:

2022-11-03

Permanent link:

<https://doi.org/10.3929/ethz-b-000579328>

Rights / license:

[In Copyright - Non-Commercial Use Permitted](#)

Originally published in:

Nature 611(7934), <https://doi.org/10.1038/s41586-022-05267-y>

Funding acknowledgement:

19-2 FEL-32 - The critical role of sedimentary trace element fluxes in ocean biogeochemistry (ETHZ)

891489 - The critical role of sedimentary trace element fluxes in ocean biogeochemistry (EC)

1 **Volcanic trigger of ocean deoxygenation during Cordilleran Ice Sheet retreat**

2 Jianghui Du^{1,2}, Alan C. Mix¹, Brian A. Haley¹, Christina L. Belanger³, Sharon³

3 ¹College of Earth, Ocean and Atmospheric Sciences, Oregon State University, Corvallis, OR,
4 97331, USA

5 ²Institute of Geochemistry and Petrology, Department of Earth Sciences, ETH Zürich,
6 Clausiusstrasse 25, 8092, Zürich, Switzerland

7 ³Department of Geology and Geophysics, Texas A&M University, College Station, TX, 77843,
8 USA

9 Corresponding author: Jianghui Du (jianghui.du@erdw.ethz.ch)

10 **North Pacific deoxygenation events during the last deglaciation were sustained over**
11 **millennia by high export productivity, but the triggering mechanisms and their links to**
12 **deglacial warming remain uncertain¹⁻³. Here we find that initial deoxygenation in the**
13 **North Pacific immediately after the Cordilleran Ice Sheet (CIS) retreat⁴ was associated**
14 **with increased volcanic ash in seafloor sediments. Timing of volcanic inputs relative to CIS**
15 **retreat suggests that regional explosive volcanism was initiated by ice unloading^{5,6}. We**
16 **posit that iron fertilisation by volcanic ash⁷⁻⁹ during CIS retreat fuelled ocean productivity**
17 **in this otherwise iron-limited region, and tipped the marine system toward sustained**
18 **deoxygenation. We also identify older deoxygenation events linked to CIS retreat over the**
19 **past ~50,000 years⁴. Our findings suggest that the apparent coupling between the**
20 **atmosphere, ocean, cryosphere and solid earth systems occurs on relatively short timescales**
21 **and can act as an important driver for ocean biogeochemical change.**

22 Reduction of dissolved oxygen (i.e., deoxygenation) in the subsurface ocean is underway and
23 projected to worsen if modern warming trends persist¹⁰. This deoxygenation will have strong
24 impacts on marine ecosystems, especially in regions that have low-oxygen backgrounds such as
25 the Oxygen Minimum Zones (OMZs) of the North and East Pacific¹¹. Identification of the
26 mechanisms that trigger and sustain long-term deoxygenation is problematic in short modern
27 observational records because of interannual-to-decadal variability¹⁰, which provides impetus for
28 study of mechanism driving past sustained ocean deoxygenation. Among the best known of such

29 occurrences are the deoxygenation events of the Northeast Pacific during the last deglacial
30 warming (19–9 thousand years ago, hereafter ka). These events, sustained for centuries-to-
31 millennia, provide a well-constrained climate context that allows investigation into the triggers
32 and impacts of deoxygenation^{1–3}.

33 The initial causes of deglacial deoxygenation events have been hypothetically linked to high-
34 latitude warming that reduced oxygen solubility, and increased metabolic oxygen demand and
35 productivity¹. However, warming alone is not sufficient to drive the entire water column to
36 deoxygenation¹². Alternative hypotheses have linked deoxygenation to slowing subsurface
37 circulation, increasing stratification, and northward advection of low-oxygen Pacific Equatorial
38 Water^{13–15}; however, deglacial circulation likely accelerated in the abyssal Pacific, while no
39 significant change of ventilation has been found at the intermediate-depths associated with
40 deoxygenation events^{16,17}. Another class of hypotheses implicates shelf iron cycling related to
41 sea-level rise as fuel for increased productivity in the iron-limited North Pacific^{3,18}. While
42 productivity and iron feedbacks may have helped to sustain deoxygenation^{1,12,19}, the initial
43 triggers remain unclear.

44 Here we document the potential role of solid earth processes in triggering the deglacial
45 deoxygenation. The solid earth is coupled to the atmosphere-ocean system through the
46 intermediary of the cryosphere on glacial-interglacial timescales; loss of ice cover can trigger
47 explosive volcanism⁵. Modern volcanic ash deposition can lead to surface phytoplankton blooms
48 in iron-limited regions including the subarctic Pacific^{7,8}. We thus hypothesise that deoxygenation
49 events in the Northeast Pacific were triggered by increasing volcanism as the Cordilleran Ice
50 Sheet (CIS) retreated during the deglacial warming.

51 To test this hypothesis, we generated high-resolution multi-tracer records of sediment
52 oxygenation at two sites in the Gulf of Alaska (GOA), Northeast Pacific. Our study sites lie
53 within the high nutrient, low chlorophyll (HNLC) region where surface water is nitrate-replete
54 but primary production is iron-limited (Fig. 1, Extended Data Fig. 1, Methods). The sites are
55 uniquely positioned at the intersection of the volcanically active Pacific “Ring of Fire”, CIS, and
56 the North Pacific HNLC and OMZ, and are thus well-suited to monitor the interactions between
57 volcanism, the cryosphere and ocean biogeochemistry. Intermediate-depth site EW0408-85JC
58 and co-located IODP Site U1419 (59.6°N, 144.2°W, 682 m water depth) sit in the upper reaches

59 of the modern OMZ and underlies North Pacific Intermediate Water. Abyssal site EW0408-87JC
60 and co-located IODP Site U1418 (58.8°N, 144.5°W, 3,680 m water depth) are presently bathed
61 by relatively well-oxygenated Pacific Deep Water that is ventilated by Southern Ocean waters¹⁶.
62 The contrast in oceanographic background at these two sites provides an additional constraint on
63 mechanisms driving deoxygenation.

64 Published highly-resolved radiocarbon-based chronologies are updated using the Marine20
65 calibration curve^{4,20,21} (Methods, Extended Data Fig. 2). We measured authigenic enrichment of
66 a suite of established redox-sensitive metals (Re, U, Cd, and Mo) in sediments at sample spacing
67 of ~90 and ~225 years for the intermediate-depth and abyssal sites respectively. The
68 exceptionally high sedimentation rate (10–1000 cm/kyr) at both sites^{4,20} diminishes the potential
69 for age offsets between authigenic accumulation and the hosting sediments to a few decades to
70 centuries (Methods). The oxygen thresholds for the enrichment of these metals roughly follow
71 the order of Re, U, Cd, and Mo²². As oxygen falls, the accumulations of Re and U increase under
72 suboxic conditions. The enrichments of Cd and Mo often require sulphidic conditions²². The use
73 of this metal suite thus allows identification of the various degrees of deoxygenation. The
74 geochemical observations are complemented by the study of the oxygen gradients inferred from
75 benthic foraminifera^{12,23}. Faunal species are classified as dysoxic, suboxic, and weakly hypoxic-
76 to-oxic, based on literature reports of their modern oxygen thresholds and multivariate ordination
77 analysis with the redox-sensitive metals (Methods).

78 To reconstruct the local volcanic input, we measured a suite of major and trace elements at the
79 intermediate-depth site, based on total sediment digestion (Methods). Volcanic fractions were
80 quantified by statistical inversion of the geochemical data²⁴ and independently supported by
81 bulk-sediment radiogenic Nd isotope (ϵ_{Nd}) evidence for sediment provenance¹⁶ (Extended Data
82 Fig. 3–5). Dispersed ash accounts for a significant portion of total ash input into marine
83 sediments²⁴. Our geochemical sensing thus provides a more complete and continuous record of
84 volcanism than is possible from visual inspection of discrete tephra layers. Because our
85 reconstructions of volcanic fraction, redox, and published paleo-temperature^{1,19} are from the
86 same samples, the stratigraphic order of warming, volcanism, and deoxygenation that we
87 establish is independent of the age model.

88 We present a new compilation of regional and global records of well-dated volcanic eruptions
89 based mainly on terrestrial tephra records (Methods), to assess the linkage between our
90 geochemical measures of volcanism from marine sediments and documented eruptions. We
91 calculate the time-varying ratio of eruptive frequency of glaciated to unglaciated volcanoes⁵
92 normalised to the Last Glacial Maximum (LGM) mean as a proxy for volcanism triggered by ice
93 unloading (Extended Data Fig. 6). We then compare the links between deoxygenation and
94 volcanism to ice sheet dynamics using well-dated records of CIS chronology, including
95 stratigraphically co-registered sedimentological evidence at the study sites⁴ and regional surface
96 exposure dates (Methods). Finally, we analysed the CIS histories reconstructed in two Glacial
97 Isostatic Adjustment (GIA) models, the global ICE-7G (VM7)²⁵ and the Northern Hemisphere
98 only LW-6²⁶, and a high-resolution three-dimensional physical ice sheet model of CIS based on
99 the Parallel Ice Sheet Model (PISM)²⁷.

100 **Timing and extent of deoxygenation**

101 The redox-sensitive metals reveal coherent temporal patterns of deglacial deoxygenation, but
102 with systematic differences in the degree of oxygenation between the intermediate-depth and
103 abyssal sites (Fig. 2). The enrichments of Mo and Cd (Fig. 2e–f) coincide with sediment
104 lamination³, indicating sulphidic conditions at the intermediate-depth site during the early
105 Bølling–Allerød (15–13.5 ka) and early Holocene (11.7–11 ka) warming intervals^{1,3,28}.
106 Enrichments of Re and U (Fig. 2c–d) show that partial deoxygenation was initiated gradually
107 starting ~17 ka, before the severe deoxygenation of Bølling warming, but after the early initial
108 warming ~21 ka indicated by regional Sea-surface temperature (SST)^{1,19} (Fig. 2a–b). Moreover,
109 Re data show persistent suboxic conditions at the intermediate-depth site throughout the
110 deglaciation (i.e., 17–10 ka) (Fig. 2c), and again intermittently during Holocene times, revealing
111 a greater duration of partial deoxygenation than previously thought^{1,3,28}. In contrast, the lack of
112 Mo enrichment and weak Cd enrichment suggests that sulphidic conditions did not reach the
113 abyssal site during the deglaciation (Fig. 2e–f). Rather, the enrichment of Re and U suggest that
114 suboxic conditions dominated at the abyssal site similarly to the intermediate-depth site (Fig. 2c–
115 d). The initiation of the deoxygenation is essentially synchronous at both sites.

116 The oxygen gradients indicated by the redox-sensitive metals are supported by benthic
117 foraminiferal species assemblages^{12,23}. Dysoxia-tolerant benthic foraminifera capture the most

118 severe deoxygenation at the intermediate-depth site corresponding to the sulphidic conditions
119 indicated by Mo and Cd (Fig. 2h). Due to the low-oxygen background at the intermediate-depth
120 site, suboxia-tolerant species are abundant except during severe deoxygenation when they are
121 replaced by dysoxia-tolerant species (Fig. 2g). The abyssal site lacks dysoxia-tolerant species,
122 while increasing abundance of suboxia-tolerant species is consistent with Re and U enrichments
123 in revealing the initiation of partial deoxygenation at ~17 ka (Fig. 2g). Redox-sensitivity metals
124 and faunal assemblages agree with each other and suggest that the development of
125 deoxygenation are coeval at both sites. This multi-proxy and multi-location consistency suggests
126 that age offsets between authigenic metals and the hosting sediments are negligible and that the
127 timing of the deoxygenation events are well captured.

128 We also find a tight coupling between deoxygenation, phytoplankton community, and surface-
129 ocean productivity exported to the seafloor based on multiple productivity proxies (Extended
130 Data Fig. 7), which we summarise using two principal components (PCs, Fig. 2i, Methods). High
131 PC2 scores indicate an early productivity increase associated with a rise in calcareous
132 plankton^{19,28} ~17 ka corresponding to the initiation of mild deoxygenation. High PC1 scores
133 show a change in the character of productivity occurred ~15 ka with high diatom export as opal
134 and elevated $\delta^{15}\text{N}$ associated with the severe deoxygenation²⁸. We suggest that an early (17–15
135 ka) improvement of the availability of surface-ocean nutrients was exploited by phytoplankton
136 groups that require warming but have modest nutrient requirements. Such an early increase in
137 productivity could have contributed to limited deoxygenation, releasing sediment-sourced
138 nutrients into the water column and making them available to the biota¹. A subsequently
139 nutrient-replete surface ocean could then host diatom blooms, which are exported more
140 efficiently to the underlying sediments to sustain severe deoxygenation.

141 The initiation of deoxygenation at ~17 ka is significantly earlier than the onset of sulphidic
142 conditions at ~15 ka. Benthic radiocarbon data indicate that deoxygenation is not associated with
143 slowing of the subsurface circulation⁴ (Extended Data Fig. 8b). A sea-surface salinity
144 reconstruction also discounts an association of meltwater and stratification with deoxygenation²⁹
145 (Extended Data Fig. 8c). Deglacial meltwater was likely mostly trapped by the Alaska Coastal
146 Current and transported alongshore to the northwest, as it is today³⁰ (Extended Data Fig. 1d).
147 Global eustatic sea-level rise is also unlikely to explain the initiation of deoxygenation^{3,18}, as

148 relative sea-level fell in the northern GOA during the deglaciation because of isostatic rebound
149 and tectonic movement^{6,31} (Extended Data Fig. 8d).

150 The early stages of deoxygenation (17–15 ka) coincided with the minimum strength of the
151 Atlantic Meridional Overturning Circulation (AMOC)³² (Extended Data Fig. 8e). This timing
152 precludes a hypothesis linking reduction in North Pacific subsurface circulation rates to
153 acceleration of AMOC¹⁵, adding to growing evidence that North Pacific variability is not a
154 passive responder to the North Atlantic but has its own dynamics^{4,29}. Mineral dust transported
155 from Asian deserts to the subpolar North Pacific remained constant during the initiation of
156 deoxygenation while decreased during the severe deoxygenation³³ (Extended Data Fig. 8f), so
157 we can reject a hypothesis that mineral dust from Asia was a primary drivers of productivity and
158 deoxygenation.

159 **Greater Volcanism following CIS retreat**

160 At the intermediate-depth site, the ϵ_{Nd} of lithogenic sediment increased rapidly starting at ~17 ka,
161 and relatively positive values persisted through the deglaciation (Fig. 3b). As volcanic materials
162 have higher ϵ_{Nd} (+6~+10)³⁴ than regional terrigenous sediments (~ -2)³⁵, more positive values of
163 ϵ_{Nd} indicate greater volcanic contributions concurrent with the initiation and development of
164 deoxygenation.

165 Statistical inversion of a broader suite of geochemical data further shows that the volcanic
166 fractions in sediments are dominated by dispersed rhyolitic ash likely sourced from the eastern
167 Aleutian Arc and/or Wrangell Volcanic Field³⁶ (Fig. 1a, Extended Data Fig. 5). The volcanic ash
168 fraction exceeded background levels at ~17 ka (Fig. 3c) and reached peak values at the beginning
169 (~16 ka and ~12 ka) of the severe deoxygenation intervals. We calculate the excess volcanic ash
170 mass accumulation rate (MAR) to be 5~100 g m⁻² yr⁻¹ (Fig. 3d), and find that it was comparable
171 to or exceeding the highest atmospheric mineral dust fluxes in the modern ocean³⁷. Given that
172 volcanic ash has similar iron solubility to mineral dust⁹, such elevated volcanic ash flux during
173 the deglacial interval could have relieved iron-limitation and fuelled biological production in the
174 Northeast Pacific.

175 Increasing deglacial volcanism on the Northeast Pacific margin is also supported by our new
176 compilation of regional and global explosive volcanism. We find that previously glaciated

177 volcanoes in the study region experienced a ~6-fold increase in activity during the deglaciation
178 relative to the LGM, significantly more than the apparent ~2-fold increase in other glaciated
179 volcanoes from elsewhere in the world (Fig. 3e, Extended Data Fig. 6). The timing of increased
180 volcanism based on the eruption frequency ratio (binned in 2-kyr intervals) is consistent with the
181 high-resolution geochemical record of dispersed ash at the intermediate-depth site. Assuming
182 that terrestrial deposition of tephra can only be preserved after the ice cover was gone, enhanced
183 deglacial volcanism could have occurred even earlier than our terrestrial compilation indicates.

184 A mechanism often used to explain the increase in volcanism during glacial retreat links ice mass
185 unloading to reduced crustal pressure and stress, and their influence on magma production and
186 storage^{5,38}. Our records indicate that regional volcanism began to increase at ~17 ka, soon after
187 the CIS started to disintegrate. Ice rafted debris (IRD) at the intermediate-depth site reveals that
188 the last major discharge event, Siku Event 1 (S1), occurred 18–17 ka (Fig. 3f), after which the
189 bulk of the CIS permanently retreated away from the Southern Alaska margin⁴. Terrestrial ¹⁰Be
190 exposure dating shows that CIS retreat was underway 19–17 ka on the Southern Alaska
191 margin³⁹, and glacial retreat in the Alaska Range began 21–18 ka with accelerating pace 17–16
192 ka⁴⁰ (Fig. 3g). Radiocarbon-based chronologies⁴¹ document an early deglaciation of the Aleutian
193 Arc (19–17 ka) and a later (15–12 ka) rapid ice loss in the Aleutian and Wrangell volcanic
194 regions (Extended Data Fig. 9a).

195 Two GIA-based models, ICE-7G²⁵ and LW-6²⁶, estimate that the majority of CIS mass loss
196 happened 15–13 ka (Fig. 3h). In ICE-7G, ice removal first started 19–17 ka in the north-western
197 part of CIS covering the Aleutian and Wrangell regions as indicated by the radiocarbon
198 chronology (Extended Data Fig. 9), consistent with our geochemical inference that these regions
199 were the likely initial source of increasing volcanism. In LW-6, the earliest CIS deglaciation
200 started 17–15 ka (Fig. 3h). This later date likely results from the model domain of LW-6
201 excluding the north-western part of the CIS²⁶.

202 In the dynamic ice sheet model PISM²⁷, significant CIS retreat could have started well before 17
203 ka, depending on which surface-temperature forcing is applied (Extended Data Fig. 10).
204 Sensitivity experiments under various temperature forcings reveal high sensitivity of ice loss to
205 local warming (-1.2 ± 0.2 metre of sea level equivalent/^oC) with a short time-lag (360 ± 213 yr).
206 Given this sensitivity, we predicted the CIS volume change when the GOA SST is applied as

207 forcing. A regional warming trend starting as early as ~21 ka predicts a much greater CIS mass
208 loss in the interval 21–17 ka and 17–15 ka (Fig. 3a, h) than suggested by the GIA-based models,
209 which have limited local sea-level data constraints particularly from the north-western side of
210 CIS. The local SST based prediction of early ice loss agrees well with the ¹⁰Be constrained CIS
211 chronology (Fig. 3g).

212 Thus, volcanism increased rapidly (~17 ka) with little time-lag (<4 kyr) following the beginning
213 of CIS unloading (starting as early as ~21 ka), consistent with the detailed case studies of Mount
214 Edgecumbe in the Southeast Alaska⁶ and modelling of magma chambers responses to ice
215 unloading³⁸.

216 **A coupled system**

217 Our results establish close links between surface warming, ice sheet retreat, volcanism, marine
218 productivity, and ocean deoxygenation during the last deglaciation on the Northeast Pacific
219 margin (Fig. 4). These linkages imply much tighter coupling of the atmosphere, ocean,
220 cryosphere, and solid earth systems, on shorter time scales than previously thought.

221 Rising summer insolation⁴² may have initiated the observed regional warming and ice sheet
222 retreat early in the deglacial sequence ~21 ka (Fig. 3a). If ice unloading induced greater volcanic
223 activity, extensive volcanic ash may in turn have accelerated ice sheet melting via the albedo
224 effects on ice ablation zones⁴³, yielding additional unloading and volcanism. Greater volcanic
225 ash input to the surface-ocean, regardless of the transport mechanism (air-fall, water or sea-ice
226 transported), would have constituted an increased flux of iron and other nutrients sufficient to
227 stimulate phytoplankton productivity ~17 ka. With sufficient deoxygenation at the seafloor, iron
228 and nutrient release from reducing sediments delivered to the upper-ocean biota by vertical
229 mixing would have fuelled further productivity and sustained deoxygenation ~15 ka¹. Diagenetic
230 mobilisation of sedimentary iron in the severe deoxygenation intervals is evidenced by
231 anomalously low paleo-magnetic intensity at the intermediate-depth site^{20,44}. Modern ocean
232 studies have documented that local marginal sources of sedimentary iron can be transported
233 through the subsurface and intermediate water circulation on basin scales throughout the
234 subpolar North Pacific, stimulating productivity and deoxygenation far-field⁴⁵. This coupled
235 Earth system thus provides a mechanism to explain the onset and long duration of deglacial
236 deoxygenation events found across the North Pacific at sites that have low-oxygen

237 backgrounds^{1,46} (Fig. 1c). Our results thus give impetus to the creation of coupled system models
238 with interactive cryosphere and solid earth components to simulate ocean biogeochemical
239 changes on orbital and millennial timescales.

240 To assess whether such events are unique to major deglaciation or happen frequently in the past,
241 we examined longer records from the same sites and found redox-sensitive metal and benthic
242 faunal evidence for brief deoxygenation events associated with earlier glacial retreats
243 documented in IRD records⁴ back to ~50 ka (Fig. 5). These older deoxygenation events typically
244 lasted a few centuries. Such transient events suggest a high sensitivity of ocean oxygenation to
245 perturbations to the coupled system on the Northeast Pacific margin.

246 Do the solid earth to ocean biogeochemistry linkages we identify here also apply to the future?
247 Much of the Cordilleran ice is gone, limiting the power of deglaciation to trigger volcanism, but
248 the remaining ice on the high elevation stratovolcanoes and other mountainous regions of the
249 Northeast Pacific margin is still significant and melting is accelerating today⁴⁷. Moreover,
250 modern global warming is putting this region in a precarious near-hypoxic state¹⁰, such that even
251 a modest increase in export productivity fuelled by volcanic iron input could amplify thermal
252 deoxygenation. It is an open question whether increased volcanism might follow from future ice
253 losses. And if so, whether it would suffice to cross deoxygenation thresholds as it did during the
254 deglaciation, or whether future deoxygenation will be strong enough to trigger sustaining
255 feedback mechanisms. Nevertheless, the linkages we have identified in the past suggest that the
256 coupling between solid earth and marine biogeochemical processes can operate relatively
257 quickly, and tipping-point behaviours exist that can sustain deoxygenation for millennia, a
258 potential concern for the future.

259 **Main references**

- 260 1. Praetorius, S. K. *et al.* North Pacific deglacial hypoxic events linked to abrupt ocean
261 warming. *Nature* **527**, 362–366 (2015).
- 262 2. Crusius, J., Pedersen, T. F., Kienast, S., Keigwin, L. & Labeyrie, L. Influence of northwest
263 Pacific productivity on North Pacific Intermediate Water oxygen concentrations during the
264 Bølling-Ållerød interval (14.7–12.9 ka). *Geology* **32**, 633–636 (2004).
- 265 3. Davies, M. H. *et al.* The deglacial transition on the southeastern Alaska Margin: Meltwater
266 input, sea level rise, marine productivity, and sedimentary anoxia. *Paleoceanography* **26**,
267 PA2223 (2011).
- 268 4. Walczak, M. H. *et al.* Phasing of millennial-scale climate variability in the Pacific and
269 Atlantic Oceans. *Science* **370**, 716–720 (2020).

- 270 5. Huybers, P. & Langmuir, C. Feedback between deglaciation, volcanism, and atmospheric
271 CO₂. *Earth Planet. Sci. Lett.* **286**, 479–491 (2009).
- 272 6. Praetorius, S. *et al.* Interaction between climate, volcanism, and isostatic rebound in
273 Southeast Alaska during the last deglaciation. *Earth Planet. Sci. Lett.* **452**, 79–89 (2016).
- 274 7. Hamme, R. C. *et al.* Volcanic ash fuels anomalous plankton bloom in subarctic northeast
275 Pacific. *Geophys. Res. Lett.* **37**, (2010).
- 276 8. Browning, T. J. *et al.* Strong responses of Southern Ocean phytoplankton communities to
277 volcanic ash. *Geophys. Res. Lett.* **41**, 2014GL059364 (2014).
- 278 9. Olgun, N. *et al.* Surface ocean iron fertilization: The role of airborne volcanic ash from
279 subduction zone and hot spot volcanoes and related iron fluxes into the Pacific Ocean.
280 *Glob. Biogeochem. Cycles* **25**, (2011).
- 281 10. Schmidtko, S., Stramma, L. & Visbeck, M. Decline in global oceanic oxygen content
282 during the past five decades. *Nature* **542**, 335–339 (2017).
- 283 11. Levin, L. A. Manifestation, Drivers, and Emergence of Open Ocean Deoxygenation. *Annu.*
284 *Rev. Mar. Sci.* **10**, 229–260 (2018).
- 285 12. Belanger, C. L., Sharon, Du, J., Payne, C. R. & Mix, A. C. North Pacific deep-sea
286 ecosystem responses reflect post-glacial switch to pulsed export productivity,
287 deoxygenation, and destratification. *Deep Sea Res. Part Oceanogr. Res. Pap.* **164**, 103341
288 (2020).
- 289 13. Hendy, I. L. & Pedersen, T. F. Is pore water oxygen content decoupled from productivity
290 on the California Margin? Trace element results from Ocean Drilling Program Hole 1017E,
291 San Lucia slope, California. *Paleoceanography* **20**, PA4026 (2005).
- 292 14. Lam, P. J. *et al.* Transient stratification as the cause of the North Pacific productivity spike
293 during deglaciation. *Nat. Geosci.* **6**, 622–626 (2013).
- 294 15. Schmittner, A., Galbraith, E. D., Hostetler, S. W., Pedersen, T. F. & Zhang, R. Large
295 fluctuations of dissolved oxygen in the Indian and Pacific oceans during Dansgaard-
296 Oeschger oscillations caused by variations of North Atlantic Deep Water subduction.
297 *Paleoceanography* **22**, (2007).
- 298 16. Du, J., Haley, B. A., Mix, A. C., Walczak, M. H. & Praetorius, S. K. Flushing of the deep
299 Pacific Ocean and the deglacial rise of atmospheric CO₂ concentrations. *Nat. Geosci.* **11**,
300 749–755 (2018).
- 301 17. Davies-Walczak, M. *et al.* Late Glacial to Holocene radiocarbon constraints on North
302 Pacific Intermediate Water ventilation and deglacial atmospheric CO₂ sources. *Earth*
303 *Planet. Sci. Lett.* **397**, 57–66 (2014).
- 304 18. Mix, A. C. *et al.* Rapid Climate Oscillations in the Northeast Pacific During the Last
305 Deglaciation Reflect Northern and Southern Hemisphere Sources. in *Mechanisms of Global*
306 *Climate Change at Millennial Time Scales* (eds. Clark, P. U., Webb, R. S. & Keigwin, L.
307 D.) 127–148 (American Geophysical Union, 1999).
- 308 19. Romero, O. E., LeVay, L. J., McClymont, E. L., Müller, J. & Cowan, E. A. Orbital and
309 Suborbital-Scale Variations of Productivity and Sea Surface Conditions in the Gulf of
310 Alaska During the Past 54,000 Years: Impact of Iron Fertilization by Icebergs and
311 Meltwater. *Paleoceanogr. Paleoclimatology* **37**, e2021PA004385 (2022).
- 312 20. Velle, J. H. *et al.* High resolution inclination records from the Gulf of Alaska, IODP
313 Expedition 341 Sites U1418 and U1419. *Geophys. J. Int.* **229**, 345–358 (2022).
- 314 21. Heaton, T. J. *et al.* Marine20—The Marine Radiocarbon Age Calibration Curve (0–55,000
315 cal BP). *Radiocarbon* **62**, 779–820 (2020).

- 316 22. Morford, J. L. & Emerson, S. The geochemistry of redox sensitive trace metals in
317 sediments. *Geochim. Cosmochim. Acta* **63**, 1735–1750 (1999).
- 318 23. Sharon, Belanger, C., Du, J. & Mix, A. Reconstructing Paleo-oxygenation for the Last
319 54,000 Years in the Gulf of Alaska Using Cross-validated Benthic Foraminiferal and
320 Geochemical Records. *Paleoceanogr. Paleoclimatology* **36**, e2020PA003986 (2021).
- 321 24. Scudder, R. P. *et al.* Geochemical approaches to the quantification of dispersed volcanic
322 ash in marine sediment. *Prog. Earth Planet. Sci.* **3**, (2016).
- 323 25. Roy, K. & Peltier, W. R. Relative sea level in the Western Mediterranean basin: A regional
324 test of the ICE-7G_NA (VM7) model and a constraint on late Holocene Antarctic
325 deglaciation. *Quat. Sci. Rev.* **183**, 76–87 (2018).
- 326 26. Lambeck, K., Purcell, A. & Zhao, S. The North American Late Wisconsin ice sheet and
327 mantle viscosity from glacial rebound analyses. *Quat. Sci. Rev.* **158**, 172–210 (2017).
- 328 27. Seguinot, J., Rogozhina, I., Stroeven, A. P., Margold, M. & Kleman, J. Numerical
329 simulations of the Cordilleran ice sheet through the last glacial cycle. *The Cryosphere* **10**,
330 639–664 (2016).
- 331 28. Addison, J. A. *et al.* Productivity and sedimentary $\delta^{15}\text{N}$ variability for the last 17,000 years
332 along the northern Gulf of Alaska continental slope. *Paleoceanography* **27**, PA1206 (2012).
- 333 29. Praetorius, S. K. *et al.* The role of Northeast Pacific meltwater events in deglacial climate
334 change. *Sci. Adv.* **6**, eaay2915 (2020).
- 335 30. Weingartner, T. J., Danielson, S. L. & Royer, T. C. Freshwater variability and predictability
336 in the Alaska Coastal Current. *Deep Sea Res. Part II Top. Stud. Oceanogr.* **52**, 169–191
337 (2005).
- 338 31. Shugar, D. H. *et al.* Post-glacial sea-level change along the Pacific coast of North America.
339 *Quat. Sci. Rev.* **97**, 170–192 (2014).
- 340 32. Ng, H. C. *et al.* Coherent deglacial changes in western Atlantic Ocean circulation. *Nat.*
341 *Commun.* **9**, 2947 (2018).
- 342 33. Serno, S. *et al.* Eolian dust input to the Subarctic North Pacific. *Earth Planet. Sci. Lett.* **387**,
343 252–263 (2014).
- 344 34. Du, J., Haley, B. A. & Mix, A. C. Neodymium isotopes in authigenic phases, bottom waters
345 and detrital sediments in the Gulf of Alaska and their implications for paleo-circulation
346 reconstruction. *Geochim. Cosmochim. Acta* **193**, 14–35 (2016).
- 347 35. Farmer, G. L., Ayuso, R. & Plafker, G. A Coast Mountains provenance for the Valdez and
348 Orca groups, southern Alaska, based on Nd, Sr, and Pb isotopic evidence. *Earth Planet. Sci.*
349 *Lett.* **116**, 9–21 (1993).
- 350 36. Preece, S. J., Westgate, J. A., Stemper, B. A. & Péwé, T. L. Tephrochronology of late
351 Cenozoic loess at Fairbanks, central Alaska. *GSA Bull.* **111**, 71–90 (1999).
- 352 37. Jickells, T. D. *et al.* Global Iron Connections Between Desert Dust, Ocean
353 Biogeochemistry, and Climate. *Science* **308**, 67–71 (2005).
- 354 38. Wilson, A. M. & Russell, J. K. Glacial pumping of a magma-charged lithosphere: A model
355 for glaciovolcanic causality in magmatic arcs. *Earth Planet. Sci. Lett.* **548**, 116500 (2020).
- 356 39. Lesnek, A. J., Briner, J. P., Lindqvist, C., Baichtal, J. F. & Heaton, T. H. Deglaciation of
357 the Pacific coastal corridor directly preceded the human colonization of the Americas. *Sci.*
358 *Adv.* **4**, eaar5040 (2018).
- 359 40. Tulenko, J. P., Briner, J. P., Young, N. E. & Schaefer, J. M. The last deglaciation of Alaska
360 and a new benchmark ^{10}Be moraine chronology from the western Alaska Range. *Quat. Sci.*
361 *Rev.* **287**, 107549 (2022).

- 362 41. Dalton, A. S. *et al.* An updated radiocarbon-based ice margin chronology for the last
363 deglaciation of the North American Ice Sheet Complex. *Quat. Sci. Rev.* **234**, 106223
364 (2020).
- 365 42. Laskar, J. *et al.* A long-term numerical solution for the insolation quantities of the Earth.
366 *Astron. Astrophys.* **428**, 261–285 (2004).
- 367 43. Muschitiello, F., Pausata, F. S. R., Lea, J. M., Mair, D. W. F. & Wohlfarth, B. Enhanced ice
368 sheet melting driven by volcanic eruptions during the last deglaciation. *Nat. Commun.* **8**,
369 1020 (2017).
- 370 44. Walczak, M. H. *et al.* A 17,000 yr paleomagnetic secular variation record from the
371 southeast Alaskan margin: Regional and global correlations. *Earth Planet. Sci. Lett.* **473**,
372 177–189 (2017).
- 373 45. Nishioka, J. *et al.* Subpolar marginal seas fuel the North Pacific through the intermediate
374 water at the termination of the global ocean circulation. *Proc. Natl. Acad. Sci.* **117**, 12665–
375 12673 (2020).
- 376 46. Jaccard, S. L. & Galbraith, E. D. Large climate-driven changes of oceanic oxygen
377 concentrations during the last deglaciation. *Nat. Geosci.* **5**, 151–156 (2012).
- 378 47. Ciraci, E., Velicogna, I. & Swenson, S. Continuity of the Mass Loss of the World’s
379 Glaciers and Ice Caps From the GRACE and GRACE Follow-On Missions. *Geophys. Res.*
380 *Lett.* **47**, e2019GL086926 (2020).
- 381 48. Boyer, T. P. *et al.* World Ocean Database 2018. A.V. Mishonov, Technical Ed., NOAA
382 Atlas NESDIS 87 (2018).
- 383 49. Global Volcanism Program, 2013. Volcanoes of the World, v. 4.8.7. (12 March 2020).
384 Venzke, E (ed.). Smithsonian Institution. <https://doi.org/10.5479/si.GVP.VOTW4-2013>.
385 (2013).
- 386 50. Veres, D. *et al.* The Antarctic ice core chronology (AICC2012): an optimized multi-
387 parameter and multi-site dating approach for the last 120 thousand years. *Clim Past* **9**,
388 1733–1748 (2013).
- 389

390 **Figure legends**

391 **Fig 1. Geology and oceanography background.** **a**, Modern land topography and ocean
392 bathymetry in the Northeast Pacific. Circles mark the intermediate-depth site EW0408-
393 85JC/IODP-U1419 and the abyssal site EW0408-87JC/IODP-U1418. **b**, Modern global surface
394 ocean nitrate concentration⁴⁸. **c, d**, Modern global ocean oxygen concentration⁴⁸ at the 700 m (**c**)
395 and 3500 m (**d**) depths respectively. In all panels, red triangles indicate Quaternary volcanoes⁴⁹.
396 The three major regional volcanic fields adjacent to the Northeast Pacific are indicated in **a**.
397 White fields show the LGM ice extent based on regional reconstruction⁴¹ (**a**) and the global ICE-
398 7G model²⁵ (**b–d**). The study region is indicated on the global maps by the black boxes.

399

400 **Fig.2 | Records of deglacial deoxygenation in the Northeast Pacific.** **a.** Greenland NGRIP ice
401 core $\delta^{18}\text{O}$ on the AICC2012 timescale⁵⁰. **b.** SST at the intermediate-depth site^{1,19} (data points
402 with 1σ uncertainty, and LOESS smoothed line with shaded 95% confidence interval/CI). **c–f,**
403 Concentrations of redox-sensitive metals normalised to Al (with 2σ uncertainties) at the
404 intermediate-depth and abyssal sites. **g** and **h,** Abundances of suboxic and dysoxic benthic
405 foraminiferal species^{12,23}. The horizontal error bars in **b–h** indicate the 95% CIs of age models.
406 The same colour legend applies to **b–h**. **i,** Principal Components of the productivity proxies from
407 the study sites; PC1 is generally associated with siliceous plankton, and PC2 with calcareous
408 plankton (Methods). The yellow bars mark sediment lamination and severe deoxygenation, and
409 the pink bars indicate milder but broader time spans of deoxygenation. The red bars at the top
410 indicate Siku Event 1 (S1)⁴.

411

412 **Fig.3 | Records of deglacial volcanism and ice sheet retreat on the Northeast Pacific margin.**
413 **a,** SST at the intermediate-depth site^{1,19} (LOESS smoothed line with shaded 95% CI), and
414 insolation on June 21th at 65°N⁴². **b,** Bulk sediment ϵ_{Nd} (points with 2σ uncertainty and LOESS
415 smoothed line with shaded 95% CI, horizontal error bars indicate the 95% CIs of age model)¹⁶. **c,**
416 Volcanic ash fraction (LOESS smoothed line with shaded 95% CI). **d,** Volcanic ash MAR in
417 excess of the background (log scale, mean values in line with 1σ range). **e,** Eruption frequency
418 ratios of glaciated volcanoes from the Northeast Pacific margin and glaciated volcanoes from
419 elsewhere in the world. Ribbons indicate interquartile ranges. **f,** IRD MAR (median with 1σ
420 range)⁴. **g,** Probability densities of ¹⁰Be age from the northern part of CIS (north of 55°N). **h,** The
421 rate of CIS volume change, in terms of sea-level equivalent, in the GIA models (LW-6²⁶ and
422 ICE-7G²⁵), and estimated using the sensitivity results of the physical ice sheet model PISM²⁷ and
423 GOA SST (median with 1σ range).

424

425 **Fig.4 | Hypothesised links between ice sheet retreat, volcanism and deoxygenation in the**
426 **Northeast Pacific.** **a,** The glacial state, with strong mass loading by the ice sheet. Volcanism is
427 depressed. Seafloor oxygenation is similar or slightly better than today and surface productivity
428 is similar or slightly weaker than today¹². **b,** The deglacial state, with increasing volcanism
429 because of ice sheet retreat, which triggered high productivity and seafloor deoxygenation at

430 both sites. OMZ likely expanded but probably did not reach the abyssal site. The albedo effect of
431 volcanic ash likely accelerated ice retreat. **c**, The interglacial state, after ice sheet retreat,
432 volcanism becomes weaker. Surface productivity and seafloor oxygenation return to baseline
433 conditions typical of the modern subpolar HNLC North Pacific. The stars mark the intermediate-
434 depth and abyssal sites.

435

436 **Fig.5 | Records of ice sheet retreat and deoxygenation on the Northeast Pacific margin in**
437 **the last 50 kyr. a.** Greenland NGRIP ice core $\delta^{18}\text{O}$ on the AICC2012 timescale⁵⁰. The Heinrich
438 Stadials are labelled. **b** and **c**, Total sediment and IRD MAR (median with 1σ range)⁴. The red
439 bars indicate Siku events⁴. **d**, Standardised concentrations (z scores, means removed) of redox-
440 sensitive metals. Thin coloured dashed lines represent individual metals. Thick pink line
441 indicates LOESS smoothing running through all metals. **e**, Abundance of dysoxic benthic
442 foraminiferal species. The yellow bars mark the deoxygenation events. The age model and MAR
443 before ~ 45 ka are beyond the limit of precise radiocarbon dating, and are thus uncertain⁴.

444

445 **Methods**

446 **Modern biogeochemistry**

447 The modern offshore GOA is part of the HNLC region of the subpolar North Pacific, where
448 moderately high surface primary production leads to incomplete utilisation of macronutrients
449 such as nitrate because of iron limitation⁵¹ (Extended Data Fig.1a–c). In contrast, the Southern
450 Alaska coastal water is a highly productive ecosystem that is iron-replete but nitrate-limited⁵².
451 These two ecological regimes are separated by the shelf break, and the two study sites,
452 85JC/U1419 on the upper slope and 87JC/U1418 on the abyssal plain, both lie within the HNLC
453 region (Extended Data Fig.1a).

454 Removal of coastal sources of Fe on the shelf is a plausible reason for low surface Fe
455 concentrations in the HNLC GOA^{52–54} (Extended Data Fig.1b). Near the coast, glacial meltwater
456 delivers Fe dominantly in particulate forms, which is rapidly removed within the inner and
457 middle shelf, trapped by the Alaska Coastal Current (ACC)⁵⁵. The fate of glacial meltwater is
458 seen in the distribution of surface salinity during the summer season (Extended Data Fig.1d). The

459 ACC traps the meltwater and transports it alongshore to the north and west, rather than
460 offshore³⁰. Through shelf-cycling, particulate Fe sustains a relatively uniform concentration of
461 dissolved Fe of a few nanomolar in the surface waters on the shelf, but the concentration
462 decreases quickly approaching the shelf break⁵⁴ (Extended Data Fig.1b). This creates a clear
463 biogeochemical boundary between the iron-replete coast/shelf waters and iron-limited HNLC
464 open ocean. Limited offshore transport of shelf-sourced Fe mainly happens via two pathways.
465 First, mesoscale eddies impinging on the shelf can deliver shelf waters to the open ocean
466 sporadically⁵⁶. Secondly, through mixing shelf-sourced Fe can enter the subsurface or even
467 intermediate waters, which are more capable of long distance transport, but this requires
468 diffusive upwelling to finally reach the surface of the HNLC regions^{45,52,57}.

469 Low atmospheric Fe deposition is another reason for low surface Fe concentration in the GOA.
470 Low dissolved Al concentration (<1 nM) in surface waters seaward of the shelf break in the
471 GOA is an indication of low atmospheric input to the HNLC region⁵⁸. Prevailing westerly winds
472 dictate that the main mineral dust source to the subpolar North Pacific is the Asian continent,
473 with decreasing deposition rate eastward³³. Despite this, glacial mineral dust is considered a
474 main source of Fe to the HNLC region as shelf Fe cannot directly reach the open ocean⁵⁹.

475 Fertilisation by volcanic ash has also been observed in the modern HNLC subpolar North
476 Pacific^{7,60}. Using an average modern mineral dust flux of 1–2 g/m²/yr³³, the total mineral dust
477 flux into the subpolar North Pacific (north of 45°N, total area of 1.02×10¹³ m²) is 10–20×10¹⁵
478 g/kyr. In comparison, long term average of volcanic ash deposition into this region from
479 surrounding subduction arcs (including Kuril, Kamchatka, Aleutian and Alaska) is estimated to
480 be 29–44×10¹⁵ g/kyr⁹. Given similar soluble Fe content⁹, this implies a comparable or greater Fe
481 source from volcanic ash than mineral dust in this region, on time scales averaged over millennia
482 or longer.

483 **Age models**

484 The age model of the intermediate-depth site was built upon 255 foraminiferal ¹⁴C dates in the
485 last 55 kyr⁴. The 85JC ¹⁴C data were mapped onto the CCSF-B depth scale of U1419 using
486 gamma-ray-attenuation bulk density (GRA) and magnetic susceptibility (MS) (Extended Data
487 Fig. 2). We update the depth conversion in ref⁴ to improve the alignment of records. To test the
488 robustness of this alignment, we deviate from our chosen depth conversion and compute the

489 resulting root mean square error (RMSE) misfits of GRA and MS between the two sites. The
490 RMSEs of GRA and MS are normalised by scaling to their respective ranges and summed given
491 equal weights. Results show that deviation of more than 1 cm will increase the misfits of GRA
492 and MS, proving that our alignment is optimal. The surface reservoir ages of samples that have
493 paired benthic-planktic ^{14}C dates were estimated using a vertical advection-diffusion box model⁴,
494 producing a transient timeseries of ΔR that averages to 120 ± 220 yr on the Marine20 timescale.
495 This average value was then applied to the planktic dates that have no benthic pairs. Benthic
496 dates were calibrated using a fixed ΔR of 860 ± 330 yr. Beyond 45 ka ^{14}C measurements have
497 large errors, and to extend the age model the IRD record of U1419 was tuned to the North
498 Atlantic IRD stack assuming a Pacific lead of 1400 yr based on the time-lag analysis after 45 ka⁴.
499 The age model of the abyssal site is anchored by 38 planktic ^{14}C dates in the last 45 kyr²⁰. The
500 87JC ^{14}C data were mapped onto the CCSF-B depth scale of U1418 using MS²⁰. The robustness
501 of the alignment is tested as described for the intermediate-depth site, and the results similarly
502 show that our alignment is optimal (Extended Data Fig. 2). Surface reservoir ages were estimated
503 following the result at the intermediate-depth site.

504 The final Bayesian age models at both sites were produced using Bchron⁶¹. We refer to refs^{4,20}
505 for the details of age model reconstruction. During the deglaciation (19–9 ka), the 1σ age model
506 uncertainty is 52 years (median, interquartile range is 47–61 years) at the intermediate-depth site,
507 and 53 years (median, interquartile range is 34–87 years) at the abyssal site. Between 19 and 55
508 ka, the 1σ age model uncertainty is 151 years (median, interquartile range is 117–217 years) at
509 the intermediate-depth site.

510 **Geochemical measurements**

511 Bulk sediment samples were digested in a CEM MARS-6 microwave using HCl-HNO₃-HF.
512 Major and trace element concentrations were measured on an ICP-OES and a quadrupole ICP-
513 MS respectively in the W.M. Keck Collaboratory for Plasma Spectrometry of Oregon State
514 University following established procedures^{34,62}. Internal standards were used to correct
515 instrumental drifts for the trace metals. Long-term (over 3 years) reproducibility was typically
516 ~2% and always <10%, monitored by repeated digestion of an in-house marine sediment
517 standard. Further quality control was done by repeated digestion of the sediment reference

518 material PACS-2 and USGS rock reference materials AGV-1, BHVO-1 and BHVO-2, which
519 agree well with literature results^{23,34}.

520 **Redox-sensitive metals**

521 Redox zonation and remobilisation in marine sediments can potentially cause depth, and thus
522 age, offsets between the location of preserved metal enrichment and the original sediment-water
523 interface (SWI) when the initial enrichment happened²². To rule out such offsets, we use multiple
524 redox-sensitive metals, which should be affected differentially by redox zonation and
525 remobilisation⁶³. We further compare the metal proxies with benthic faunal proxies, which are
526 not affected by such offsets^{12,23}. The result that the timings of deoxygenation are the same
527 indicated by different metals and benthic faunas confirms that zonation and remobilisation are
528 not important at the study sites. Offsets in age are minimised by high sedimentation rates at both
529 sites, which vary from 10 to 1000 cm/kyr in the last 55 ka and are amongst the highest reported
530 at similar water depths^{4,20}. Previous studies have showed that Re enrichment is ~1 cm offset from
531 the SWI in suboxic and sulphidic sediments, while the Mo enrichment is ~0.2 cm offset from the
532 SWI in sulphidic sediments⁶⁴. Such depth offsets correspond to <100 yr age offsets at our study
533 sites. High sedimentation rates not only reduce age offset due to zonation, but also prevents
534 remobilisation by reducing oxygen exposure time⁶³. Rhenium is likely the most sensitive to
535 reoxidation⁶³, but the strong correlation to other redox metals and the benthic faunas rules out
536 remobilisation as a significant process at the study sites. Moreover, enrichment of these metals in
537 sediment can happen due to non-redox related processes, for example, being carried by Fe-Mn
538 oxides and biogenic materials to sediments²². The use of multiple metals together with the
539 benthic faunas thus helps minimise such potential biases.

540 Based on the age models, our deglacial (19–9 ka) redox-sensitive metal sample spacing is 90
541 years (median, interquartile range is 53–151 years) at the intermediate-depth site and 225 years
542 (median, interquartile range is 73–360 years) at the abyssal site. Between 19 and 55 ka, the
543 sample spacing is 112 years (median, interquartile range is 55–200 years) at the intermediate-
544 depth site. Considering the high sampling resolutions, low age model uncertainties and small age
545 offsets, we argue the redox-sensitive metals can constrain the timing of deoxygenation events to
546 ~100 years at the study sites during the deglaciation and a few centuries during the glacial
547 period.

548 **Benthic foraminifera assemblages**

549 Benthic foraminifera data have been published previously, where species were classified as
550 dysoxic ($O_2 < 0.5$ ml/L), suboxic (0.5–1 ml/L), and weakly hypoxic-to-oxic (> 1 ml/L) based on
551 literature values of oxygen thresholds and multivariate ordination analysis^{12,23}. The dysoxic
552 species dominate under the sulphidic conditions of Mo and Cd enrichment, the suboxic species
553 are prevalent under the mildly reducing condition of Re and U enrichment, while the weakly
554 hypoxic-to-oxic species represent the low-oxygen background that is not sufficient to cause
555 authigenic metal enrichment.

556 **Sea-surface temperatures**

557 Published sea-surface temperatures reconstructed using $U^{K'}_{37}$ at the intermediate-depth site 85JC¹
558 and U1419¹⁹ are here placed on the unified and updated Marine20 based age model^{4,21}. The
559 deglacial $U^{K'}_{37}$ records from the two sites are offset following a relationship of $U^{K'}_{37}(85JC) =$
560 $0.94 \times U^{K'}_{37}(U1419) - 0.01$ ($r=0.9$, $p < 0.05$), likely reflecting inter-laboratory offsets. We
561 corrected the published U1419 record to be consistent with that of 85JC, and converted $U^{K'}_{37}$ to
562 SST using the calibration program BAYSPLINE⁶⁵. The analytical $U^{K'}_{37}$ offset of 0.03 ($1\sigma = 0.01$)
563 between 85JC and U1419 is equivalent to a SST difference of 0.75°C ($1\sigma = 0.19^\circ\text{C}$) using this
564 calibration, which is smaller than the 1.35°C (1σ) uncertainty of the calibration itself.

565 **Productivity proxies**

566 Ocean and sedimentary processes can potentially cause productivity proxies to not accurately
567 record paleo-productivity signals, including poor preservation, overprinting of other
568 environmental factors and differing responses of phytoplankton communities^{66,67}. We thus adopt
569 a multi-proxy approach to provide a more complete picture of productivity change at the study
570 sites during the deglaciation (Extended Data Fig. 7).

571 High CaCO_3 concentrations at the intermediate-depth site are found during the mild
572 deoxygenation intervals, but not the severe deoxygenation intervals (Extended Data Fig. 7a).
573 Sediment Sr/Al ratios (Extended Data Fig. 7b) are correlated to CaCO_3 concentrations and thus
574 can be used as a proxy for CaCO_3 in the study region. It shows that the patterns of CaCO_3
575 variations at the intermediate-depth and abyssal sites are similar, with the productivity increase
576 beginning at ~ 17 ka. The correlation of CaCO_3 concentration with coccolith counts (Extended
577 Data Fig. 7c) suggests that the increase in productivity during the mild deoxygenation intervals

578 were partly driven by calcareous plankton. Sediment CaCO₃ may be affected by dissolution. A
579 previous study found evidence of enhanced dissolution at the intermediate-depth site during the
580 severe deoxygenation intervals but not during the mild deoxygenation intervals⁶⁸. Carbonate
581 dissolution is expected to be stronger at the abyssal site, and thus the increase in calcareous
582 productivity indicated here is likely underestimated.

583 High total organic carbon (TOC) and biogenic opal concentrations at the intermediate-depth site
584 indicate high productivity during the severe deoxygenation intervals (Extended Data Fig. 7d–e).
585 However, during the onset of deoxygenation at 17–15 ka, TOC and opal may not record the
586 moderate productivity increase because of poor preservation, dilution by lithogenic sediments, or
587 because diatoms require nutrient-replete conditions, which were likely not prevalent until the
588 productivity-deoxygenation feedback is fully established in the severe deoxygenation intervals.

589 The bulk sediment organic matter $\delta^{15}\text{N}$ at the intermediate-depth site was corrected for terrestrial
590 organic input to indicate marine organic matter $\delta^{15}\text{N}^{28}$ (Extended Data Fig. 7f). High $\delta^{15}\text{N}$
591 indicates greater surface-ocean nutrient utilisation or sediment denitrification during the severe
592 deoxygenation intervals, and the initial increase at ~17 ka is consistent with the early increase in
593 productivity corresponding to the early onset of deoxygenation indicated by Re.

594 Sediment Ba/Al ratios at the intermediate-depth site are correlated to opal concentrations,
595 reflecting the high productivity during the severe deoxygenation intervals (Extended Data Fig.
596 7g). However, barite is under-saturated in the water column at intermediate depths in the North
597 Pacific⁶⁹, and barite dissolution in sediments may happen at suboxic conditions and strongly so
598 under sulphidic conditions⁷⁰. Biogenic Ba to carbon ratios also increase with water depth⁷¹. Thus,
599 Ba/Al ratios at the intermediate-depth site are lower than at the abyssal site in the subpolar North
600 Pacific⁶⁶, and likely only record the very high diatom-dominated productivity during the severe
601 deoxygenation intervals but not the moderate increase in productivity during the onset of
602 deoxygenation. The abyssal site Ba/Al ratio is likely less affected by under-saturation and
603 diagenesis, and captures the rise of productivity at ~17 ka as well as throughout the
604 deoxygenation consistent with the increase in suboxic benthic foraminiferal species.

605 Increases in the abundance of benthic foraminiferal species linked to organic detritus indicates
606 the initial rise of productivity 17–15 ka (Extended Data Fig. 7h). The benthic species we show
607 are *Islandiella norcrossi* at the intermediate-depth site and *Elphidium batialis* at the abyssal

608 site. *Islandiella norcrossi* thrives under highly productive waters near seasonal sea ice margin⁷².
609 It, however, is a shallow water species that is normally not found in deep-sea
610 sediments. *Elphidium batialis* is phytophagous⁷³ and only found at the abyssal site. Both species
611 became the most abundant taxon at their respective sites in 17–15 ka but are outcompeted when
612 more severe deoxygenation prevails.

613 We summarised the productivity proxies using Principal Component Analysis (PCA)^{74,75}. The
614 coccolith counts are excluded in PCA because of low sample resolution. PC1 (34%) and PC2
615 (30%) account for the majority of total variance in the proxy data (Fig. 2i). PC1 has high
616 loadings on opal, TOC and Ba/Al ratio from the intermediate-depth site, with its high scores
617 indicating diatom driven high productivity during severe deoxygenation. PC2 has high loadings
618 on CaCO₃ and Sr/Al ratio from both sites, with its high scores indicating the moderately high
619 productivity increase during the mild deoxygenation intervals, likely driven by calcareous
620 phytoplankton growth.

621 **Geochemical provenance analysis**

622 The Gulf of Alaska is surrounded by three major volcanic fields: the Aleutian Arc (AA), the
623 Wrangell Volcanic Field (WVF) and the North Cordilleran Volcanic Field (NCVF), as well as
624 many other small volcanic centres (Fig. 1a). To estimate the volcanic fraction in sediments at the
625 intermediate-depth site, we first identify the volcanic endmembers. Because volcanic materials
626 from different volcanoes often overlap in geochemistry, and the erupted materials of the same
627 volcano often evolve geochemically over time, we do not seek to fingerprint the individual
628 volcanoes that produced the volcanic materials found at our sites, but instead we seek
629 endmembers that are clearly defined by geochemistry²⁴.

630 We derive geochemical endmembers by analysing the Alaska Volcano Observatory (AVO)⁷⁶ and
631 the GEOROC⁷⁷ databases. AVO is a comprehensive collection of Quaternary volcanic samples
632 in the State of Alaska, US. AA and WVF are represented in this database. GEOROC is a
633 collection of global igneous rock samples. We used the samples from Yukon and British
634 Columbia, Canada, in the precompiled North America Cordillera (Cenozoic to Quaternary) sub-
635 database, including samples from NCVF. We extracted major and trace element data of volcanic
636 materials including glass (tephra) and whole rock analyses. We performed cluster analysis using
637 the following set of elements: SiO₂, TiO₂, Al₂O₃, FeO_T, MnO, MgO, CaO, Na₂O, K₂O, Rb, Ba,

638 Sr, La, Ce, Nd, Eu, Tb, Ho, Yb, Zr, Nb, as a reasonable compromise to maximise both the
639 number of samples and the number of elements (most samples only have limited numbers of
640 elements reported). In total, 2273 unique samples were included. We performed hierarchical
641 cluster analysis using the complete-linkage method⁷⁸ with the Aitchison distance⁷⁹ (equivalent to
642 using the Euclidean distance on isometric-log-ratio transformed data), which is ideal for
643 compositional data analysis because it resolves the “closure problem”.

644 We identified 5 major volcanic clusters (rare clusters smaller than 2% of the total samples were
645 ignored), and the geochemical distinctions are shown in a Total Alkali Silica (TAS) diagram, a
646 Rare Earth Element (REE) pattern and a trace element spidergram (Extended Data Fig. 3). The
647 clusters are defined as (in the order of decreasing size): basalt–andesite-dacite; basalt (tholeiitic);
648 basalt (alkaline); rhyolite (adakite), and rhyolite (typical arc). While the clusters are not unique to
649 any specific volcanoes, general correspondence does exist: (1) Quaternary tephra samples in
650 Alaska mainly fall into the rhyolite clusters, which are separated into a “typical arc” cluster and
651 an adakite cluster with the latter characterized by greater light REE enrichment. These two
652 clusters are commonly known as the type-I and type-II ashes in Alaska tephrochronology^{80,81}.
653 The typical arc cluster mostly originates from the central AA, while the adakite cluster mostly
654 comes from WVF and the Alaska Peninsula (the eastern AA). (2) The basalt–andesite-dacite
655 cluster represents the main volcanic rock and lava series of the AA, though it is common
656 elsewhere too. Some deglacial terrestrial and marine tephra found on the Southern Alaska margin
657 belong to this cluster^{6,82}. (3) The basalt (alkaline) cluster is mainly found in the NCVF⁸³, as well
658 as some volcanic centres in the Bering Sea. We calculated the geometric means of each cluster
659 and used them as the final geochemical endmembers of volcanic materials for purposes of linear
660 mixing modelling later.

661 Next, we define the terrigenous endmembers. Provenance studies based on thermochronology^{84–}
662 ⁸⁶, zircon geochemistry⁸⁴ and heavy minerals⁸⁷ show that the Pleistocene terrigenous sediments
663 at the intermediate-depth and abyssal sites are mainly delivered by the Bagley-Bering Glacier
664 system, which brings eroded materials from the Cretaceous-Eocene accretionary complex of the
665 Chugach-Prince William (CPW) terrane⁸⁸. The CPW terrane includes the Valdez and Orca
666 groups consisted mainly of metasedimentary rocks and minor metabasite rocks, with increasing
667 degree of metamorphism toward the Chugach Metamorphic Complex (CMC) eastward in the

668 Saint Elias Mountains. These terranes are intruded by the Palaeocene-Eocene Sanak-Baranof
669 Plutonic Belt (SBPB).

670 We compiled published major and trace element data of these terrestrial geological
671 endmembers^{89–95}. We calculated the Aitchison distances between the geological endmembers
672 and the Holocene (<10 ka) and Glacial (22–17 ka) sediment samples at the intermediate-depth
673 site (outside the intervals of deglacial deoxygenation) using the following set of elements: TiO₂;
674 Al₂O₃; FeO_T; MnO; MgO; Na₂O; K₂O; La; Ce; Nd; Eu; Tb; Yb; Zr, representing a compromise
675 between maximising the number of samples and the number of elements included. Potentially
676 biogenic elements in marine sediments (Si, Ca, Ba and Sr) were not included. The Aitchison
677 distance helps to identify the similarity between GOA sediments and the potential terrigenous
678 endmembers.

679 Previous studies found that the terrigenous sediment provenance on the Southern Alaska margin
680 has been stable since the Pleistocene^{84–87}. This is borne out by the statistically indistinguishable
681 bulk sediment ϵ_{Nd} at the intermediate-depth site between the Glacial and the Holocene samples
682 (Fig. 3b), suggesting that the geochemical changes during the deglaciation were not driven by
683 changes in terrigenous sediment provenance, but instead reflect changes in other lithogenic
684 inputs (*i.e.*, volcanic ash). Consistently, the major and trace element data (Extended Data Fig. 4)
685 show that Glacial and Holocene sediments at the intermediate-depth site lie within the
686 geochemical space spanned by the potential terrigenous endmembers, and that internal
687 differences between the Glacial and Holocene sediments are negligible when compared with the
688 differences between the GOA sediments and the potential terrigenous endmembers. This finding
689 indicates stability of background terrigenous sediment provenance despite the changes in
690 sedimentation and erosion rates from the LGM to the Holocene⁴.

691 We are interested in the *relative* partitioning of volcanic and terrigenous sediments. The stability
692 of the terrigenous sediment provenance implies that the terrigenous sediments can be effectively
693 treated as a near constant mixture, consistent in Holocene and Glacial sediments. Thus, we take
694 the compositions of the Holocene and Glacial sediments as *heuristic* terrigenous endmembers.
695 This approach allows us to partition terrigenous sediments relative to volcanic sediments within
696 reasonable uncertainties without a comprehensive partitioning of the terrigenous provenance (the
697 endmembers of which are less-well geochemically constrained).

698 **Geochemical data inversion**

699 The distinct geochemistry of volcanic endmembers and the apparent stability of the terrigenous
700 sediment provenance allow us to quantify their contributions to marine sediments at the
701 intermediate-depth site using geochemical inversion²⁴. We interpret the inversion results based
702 on the well-established geochemical characterisation of volcanic, particularly ash, sources in the
703 Alaska tephrochronology^{80,81}.

704 The geochemical provenance analysis at the intermediate-depth site is formulated as the inverse
705 problem of a constrained linear mixing model:

706 Minimise $\|(\mathbf{Ax}-\mathbf{b})/\boldsymbol{\delta}\|_2$, subject to $\Sigma\mathbf{x} = 1$ and $\mathbf{x} \geq 0$, (1)

707 Here \mathbf{A} is the matrix consists of multidimensional elemental concentrations of the endmembers,
708 in which each column is an endmember and each row is an element. \mathbf{b} is the elemental
709 concentrations of a sediment sample, and \mathbf{x} is the mixing fractions of the endmembers to be
710 solved, which are non-negative and sum to one. $\boldsymbol{\delta}$ is the weighting vector consists of the external
711 standard deviations of the elements resulting from repeated digestion and analysis of the
712 reference materials. In total, 26 elements (Al_2O_3 , MgO , Na_2O , K_2O , FeO_T , MnO , TiO_2 , Cr , Cu ,
713 Ni , Zn , all 14 REEs and Zr) were used. Bulk sediment ϵ_{Nd} was *not* used in the mixing model, but
714 it serves as an independent check on the reconstruction of volcanic fraction.

715 Elemental concentrations of sediment samples were first normalised to a 100% lithogenic
716 fraction basis. Biogenic (organic matter, carbonate and opal) and lithogenic fractions at the
717 intermediate-depth site were previously measured on selected samples²⁸. From these data, we
718 derived a multiple linear regression to estimate the lithogenic fractions using density, Al, Ca and
719 Ba concentrations as predictors ($r^2=0.9$, $p \ll 0.05$). Sediments on the Southern Alaska margin are
720 predominantly lithogenic⁹⁶, and at the intermediate-depth site the lithogenic fractions varied little
721 since the LGM (90 ± 3 wt%)²⁸, making this correction minor. Finally, the results of the inversion
722 give the weight fractions of the volcanic and terrigenous endmembers within lithogenic
723 sediments, which are then converted back to weight fractions within the total sediments. We
724 solved problem (1) using a linear least square algorithm with non-negativity constraint⁹⁷.

725 The rhyolite (adakite), rhyolite (typical arc) and basalt (alkaline) endmembers all had their
726 greatest relative abundance during the deglaciation (Extended Data Fig. 5). The dominance of

727 the two rhyolite ash endmembers is consistent with the depositional patterns of ash plumes
728 during modern eruptions⁹⁸, and in agreement with the dominance of these two clusters in the
729 Quaternary terrestrial tephrochronology of Alaska^{80,81}. The implication is that the eastern portion
730 of AA and WVF were more active during the deglaciation. The minor increase in the basalt
731 (alkaline) endmember may be attributed to greater input from the NCVF or the volcanic centres
732 in the Bering Sea. The lack of correlation between ash abundance and sediment MAR shows that
733 the variation of the ash fraction was not compromised by a dilution effect (Extended Data Fig.
734 5b). The constancy of the volcanic ash fraction between the LGM and the Holocene, despite
735 changes in sediment MAR, suggests a “background ash” fraction of ~7%. We then calculated the
736 excess volcanic ash fractions and fluxes after removing this background.

737 **Global and regional records of deglacial volcanism**

738 We compiled published global and regional records of volcanic eruptions since the LGM. Our
739 compilation includes the Global Volcanism Program (GVP) database⁴⁹, the Bryson et al., 2006
740 (B06) radiocarbon database⁹⁹, the Watt et al., 2013 (W13) selected volcanic arc database¹⁰⁰, the
741 Large Magnitude Explosive volcanic Eruptions (LaMEVE) database¹⁰¹, the Alaska Volcano
742 Observatory eruption database⁷⁶, and other recent studies in Alaska^{6,82,102}. The previous global
743 compilation of Huybers and Langmuir, 2009 (HL09)⁵ was based on B06 and an older version of
744 GVP. Our new compilation updated GVP while also included LaMEVE and AVO as well as
745 other recent data, which increased the deglacial coverage. We removed duplicates among the
746 databases, standardised the volcano names and added the unique volcano numbers following the
747 GVP convention. This makes the compilation traceable and easier for future extension. In HL09,
748 small magnitude eruptions ($VEI \leq 2$) in GVP were removed, but we choose to keep all eruptions
749 in our compilation for consistency’s sake since eruption magnitudes were rarely reported. In
750 total, there are 12,403 events reported since 24 ka. Following HP09, we assigned a standard
751 deviation equal to 10% of the reported age when age errors were not available (excluding
752 historical observations that were assumed to be precisely dated). We recalibrated radiocarbon
753 dates using Bchron⁶¹ with IntCal20¹⁰³ whenever raw dates were available.

754 We identify glaciated volcanoes using the modern ice volume balance following HL09, which
755 assumes that previously glaciated regions likely have less negative ice volume balance today.
756 The modern ice volume balance is calculated using the NCEP/NCAR Reanalysis of precipitation

757 and temperature¹⁰⁴, and volcanoes that have a modern ice volume balance > -9 m/yr are
758 considered glaciated like HL09. Eruption events were binned into 2-kyr intervals (Extended Data
759 Fig. 6). Like HL09, we assumed that the temporal sampling biases of eruption events in the
760 glaciated and unglaciated volcano datasets are the same. Thus, the eruption frequency ratio of the
761 glaciated volcanoes to the unglaciated ones may remove this bias, and can be used as a proxy for
762 glaciation-induced volcanism. Finally, we normalised the eruption frequency ratio relative to the
763 LGM mean ratio (22–24 ka), which diverged from HL09 who chose to normalise to the last 2
764 kyr. We believe the LGM-normalisation is likely a less biased normaliser because while the
765 numbers of eruption events during the LGM and deglacial are within one order of magnitude
766 (Extended Data Fig. 6), two orders of magnitude more eruptions are recorded in the last 2 kyr.
767 The difference in sampling bias between the LGM and the deglaciation is presumably smaller
768 than between them and the last 2 kyr. Our results thus address the question “Was deglacial
769 volcanism more active than that of the LGM?” rather than the question “Was deglacial
770 volcanism more active than that of the last 2 kyr”, as originally investigated by HL09.
771 Regardless, the choice of normalisation will affect the absolute magnitude, but not the relative
772 change, of the eruption frequency ratio. To evaluate the impact of dating uncertainties, binning
773 and ratioing was performed 1000 times in Monte-Carlo simulations including Gaussian
774 distributions of ages for each eruption event.

775 **Beryllium-10 exposure dates**

776 We compiled published ¹⁰Be exposure dates from the regions that were previously covered by
777 the northern part of the CIS (north of 55°N) surrounding the GOA, including the South Alaska
778 margin^{39,105–107}, the Alaska Range^{40,108,109} and the interior of CIS^{110,111}. We calculated the
779 weighted average and standard deviation of ¹⁰Be age at each sample site. We then computed the
780 probability density of the age distribution at each of the three regions using kernel density
781 estimation¹¹², giving equal weight to each sample site within the same region. Finally, we
782 summed the probability density of all three regions, giving equal weight to each region.

783 **CIS in PISM sensitivity experiments**

784 We analysed the sensitivity of CIS volume to the surface temperature forcing in the PISM
785 experiments performed by Seguinot et al, (2016)^{27,113} (<https://zenodo.org/record/3606536>).
786 Lacking regional surface temperature records suitable for CIS experiments, Seguinot et al

787 applied hypothetical surface temperature forcing scaled to other temperature records, including
788 the Greenland GRIP¹¹⁴ and NGRIP¹¹⁵ ice core records, the Antarctic EPICA¹¹⁶ and VOSTOK¹¹⁷
789 ice core records, and SST records from the California margin sites ODP 1012 and ODP 1020¹¹⁸.
790 The temperature records were scaled to anomalies that have average glacial (22–32 ka)
791 temperature 6–7°C lower than today²⁷ (Extended Data Fig. 10a). We identified the deglacial
792 time-lag of the ice volume response to temperature forcing by computing the cross-correlation of
793 the 0–26 ka part of the ice volume and temperature time-series (except for the sensitivity
794 experiment using the ODP 1012 SST forcing, which has a much earlier deglaciation, and we thus
795 used the 6–32 ka part of the time-series) (Extended Data Fig. 10d). The average time-lag is
796 468 ± 362 yr (1σ) when including all 8 sensitivity experiments. However, the experiments using
797 the ODP 1012 SST forcing appears a outlier as the ice volume response is inconsistent with ice
798 sheet reconstructions²⁷. Excluding this outlier, the average time-lag is 360 ± 213 yr (1σ). Linear
799 regression between ice volume and lagged temperature gives a sensitivity of an ice loss of
800 1.2 ± 0.2 (1σ) metre of sea level equivalent per 1°C of warming (Extended Data Fig. 10e).

801 Based on the ice volume-temperature relationship in the sensitivity experiments, we estimated
802 the CIS volume response had the GOA SST record been used as the temperature forcing
803 (Extended Data Fig. 10f). The GOA SST record is scaled to have a glacial temperature anomaly
804 of -6°C consistent with the sensitivity experiments. We then predict the CIS response to GOA
805 SST forcing using the time-lagged linear regression results from the sensitivity experiments
806 (Extended Data Fig. 10e). We perform 10,000 Monte Carlo sampling to propagate errors
807 including the errors of the SST calibration and the uncertainties of the time-lag and ice sheet
808 response in the PISM sensitivity experiments (Fig. 3h, Extended Data Fig. 10f).

809 **Data Availability**

810 The geochemical datasets generated by this study and the data compilations are publicly
811 available (<https://doi.org/10.5281/zenodo.6770651>). Source data are provided with this paper.

812 **Code availability**

813 Computer codes used in the study are publicly available
814 (<https://doi.org/10.5281/zenodo.6770651>).

815 **Methods references**

- 816 51. Martin, J. H., Gordon, R. M., Fitzwater, S. & Broenkow, W. W. Vertex: phytoplankton/iron
817 studies in the Gulf of Alaska. *Deep Sea Res. Part Oceanogr. Res. Pap.* **36**, 649–680 (1989).
- 818 52. Lippiatt, S. M., Lohan, M. C. & Bruland, K. W. The distribution of reactive iron in northern
819 Gulf of Alaska coastal waters. *Mar. Chem.* **121**, 187–199 (2010).
- 820 53. Aguilar-Islas, A. M. *et al.* Temporal variability of reactive iron over the Gulf of Alaska
821 shelf. *Deep Sea Res. Part II Top. Stud. Oceanogr.* **132**, 90–106 (2016).
- 822 54. Crusius, J., Schroth, A. W., Resing, J. A., Cullen, J. & Campbell, R. W. Seasonal and
823 spatial variabilities in northern Gulf of Alaska surface water iron concentrations driven by
824 shelf sediment resuspension, glacial meltwater, a Yakutat eddy, and dust. *Glob.*
825 *Biogeochem. Cycles* **31**, 942–960 (2017).
- 826 55. Wu, J. *et al.* Size-fractionated iron distribution on the northern Gulf of Alaska. *Geophys.*
827 *Res. Lett.* **36**, (2009).
- 828 56. Brown, M. T., Lippiatt, S. M., Lohan, M. C. & Bruland, K. W. Trace metal distributions
829 within a Sitka eddy in the northern Gulf of Alaska. *Limnol. Oceanogr.* **57**, 503–518 (2012).
- 830 57. Lam, P. J. *et al.* Wintertime phytoplankton bloom in the subarctic Pacific supported by
831 continental margin iron. *Glob. Biogeochem. Cycles* **20**, GB1006 (2006).
- 832 58. Brown, M. T., Lippiatt, S. M. & Bruland, K. W. Dissolved aluminum, particulate
833 aluminum, and silicic acid in northern Gulf of Alaska coastal waters: Glacial/riverine inputs
834 and extreme reactivity. *Mar. Chem.* **122**, 160–175 (2010).
- 835 59. Crusius, J. Dissolved Fe Supply to the Central Gulf of Alaska Is Inferred to Be Derived
836 From Alaskan Glacial Dust That Is Not Resolved by Dust Transport Models. *J. Geophys.*
837 *Res. Biogeosciences* **126**, e2021JG006323 (2021).
- 838 60. Duggen, S., Croot, P., Schacht, U. & Hoffmann, L. Subduction zone volcanic ash can
839 fertilize the surface ocean and stimulate phytoplankton growth: Evidence from
840 biogeochemical experiments and satellite data. *Geophys. Res. Lett.* **34**, (2007).
- 841 61. Haslett, J. & Parnell, A. A simple monotone process with application to radiocarbon-dated
842 depth chronologies. *J. R. Stat. Soc. Ser. C Appl. Stat.* **57**, 399–418 (2008).
- 843 62. Muratli, J. M., McManus, J., Mix, A. & Chase, Z. Dissolution of fluoride complexes
844 following microwave-assisted hydrofluoric acid digestion of marine sediments. *Talanta* **89**,
845 195–200 (2012).
- 846 63. Crusius, J. & Thomson, J. Comparative behavior of authigenic Re, U, and Mo during
847 reoxidation and subsequent long-term burial in marine sediments. *Geochim. Cosmochim.*
848 *Acta* **64**, 2233–2242 (2000).
- 849 64. Crusius, J., Calvert, S., Pedersen, T. & Sage, D. Rhenium and molybdenum enrichments in
850 sediments as indicators of oxic, suboxic and sulfidic conditions of deposition. *Earth Planet.*
851 *Sci. Lett.* **145**, 65–78 (1996).
- 852 65. Tierney, J. E. & Tingley, M. P. BAYSPLINE: A New Calibration for the Alkenone
853 Paleothermometer. *Paleoceanogr. Paleoclimatology* **33**, 281–301 (2018).
- 854 66. Serno, S. *et al.* Using the natural spatial pattern of marine productivity in the Subarctic
855 North Pacific to evaluate paleoproductivity proxies. *Paleoceanography* **29**, 2013PA002594
856 (2014).
- 857 67. Lopes, C., Kucera, M. & Mix, A. C. Climate change decouples oceanic primary and export
858 productivity and organic carbon burial. *Proc. Natl. Acad. Sci.* **112**, 332–335 (2015).
- 859 68. Payne, C. R. & Belanger, C. L. Enhanced carbonate dissolution associated with deglacial
860 dysoxic events in the subpolar North Pacific. *Paleoceanogr. Paleoclimatology* **36**,
861 e2020PA004206 (2021).

- 862 69. Rushdi, A. I., McManus, J. & Collier, R. W. Marine barite and celestite saturation in
863 seawater. *Mar. Chem.* **69**, 19–31 (2000).
- 864 70. McManus, J. *et al.* Geochemistry of barium in marine sediments: implications for its use as
865 a paleoproxy. *Geochim. Cosmochim. Acta* **62**, 3453–3473 (1998).
- 866 71. Dymond, J., Suess, E. & Lyle, M. Barium in Deep-Sea Sediment: A Geochemical Proxy for
867 Paleoproductivity. *Paleoceanography* **7**, 163–181 (1992).
- 868 72. Seidenkrantz, M.-S. Benthic foraminifera as palaeo sea-ice indicators in the subarctic realm
869 – examples from the Labrador Sea–Baffin Bay region. *Quat. Sci. Rev.* **79**, 135–144 (2013).
- 870 73. Fontanier, C. *et al.* Living (stained) deep-sea foraminifera off Hachinohe (NE Japan,
871 Western Pacific): Environmental interplay in oxygen-depleted ecosystems. *J. Foraminifer.*
872 *Res.* **44**, 281–299 (2014).
- 873 74. Lê, S., Josse, J. & Husson, F. FactoMineR: An R Package for Multivariate Analysis. *J. Stat.*
874 *Softw.* **25**, 1–18 (2008).
- 875 75. Josse, J. & Husson, F. missMDA: A Package for Handling Missing Values in Multivariate
876 Data Analysis. *J. Stat. Softw.* **70**, 1–31 (2016).
- 877 76. Cameron, C. E., Mulliken, K. M., Crass, S. W., Schaefer, J. R., and Wallace, K. L. Alaska
878 Volcano Observatory geochemical database, version 2: Alaska Division of Geological &
879 Geophysical Surveys Digital Data Series 8 v. 2, 22 p. <http://doi.org/10.14509/30058> (2019).
- 880 77. Sarbas, B., Jochum, K. P., Nohl, U. & Hofmann, A. W. GEOROC, the MPI geochemical
881 rock database: a new tool for geochemists. *Eos Trans. AGU* **80**, F1184 (1999).
- 882 78. Templ, M., Filzmoser, P. & Reimann, C. Cluster analysis applied to regional geochemical
883 data: Problems and possibilities. *Appl. Geochem.* **23**, 2198–2213 (2008).
- 884 79. Egozcue, J. J., Pawlowsky-Glahn, V., Mateu-Figueras, G. & Barceló-Vidal, C. Isometric
885 Logratio Transformations for Compositional Data Analysis. *Math. Geol.* **35**, 279–300
886 (2003).
- 887 80. Preece, S. J., Westgate, J. A., Froese, D. G., Pearce, N. J. G. & Perkins, W. T. A catalogue
888 of late Cenozoic tephra beds in the Klondike goldfields and adjacent areas, Yukon
889 Territory1Yukon Geological Survey Contribution 010. *Can. J. Earth Sci.* **48**, 1386–1418
890 (2011).
- 891 81. Westgate, J. A., Perkins, W. T., Fuge, R., Pearce, N. J. G. & Wintle, A. G. Trace-element
892 analysis of volcanic glass shards by laser ablation inductively coupled plasma mass
893 spectrometry: application to tephrochronological studies. *Appl. Geochem.* **9**, 323–335
894 (1994).
- 895 82. Wilcox, P. S. *et al.* A new set of basaltic tephtras from Southeast Alaska represent key
896 stratigraphic markers for the late Pleistocene. *Quat. Res.* **92**, 246–256 (2019).
- 897 83. Edwards, B. R. & Russell, J. K. Northern Cordilleran volcanic province: A northern Basin
898 and Range? *Geology* **27**, 243–246 (1999).
- 899 84. Huber, B., Bahlburg, H., Berndt, J., Dunkl, I. & Gerdes, A. Provenance of the Surveyor Fan
900 and Precursor Sediments in the Gulf of Alaska—Implications of a Combined U-Pb, (U-
901 Th)/He, Hf, and Rare Earth Element Study of Detrital Zircons. *J. Geol.* **126**, 577–600
902 (2018).
- 903 85. Dunn, C. A., Enkelmann, E., Ridgway, K. D. & Allen, W. K. Source to sink evaluation of
904 sediment routing in the Gulf of Alaska and Southeast Alaska: A thermochronometric
905 perspective. *J. Geophys. Res. Earth Surf.* **122**, 711–734 (2017).

- 906 86. Bootes, N., Enkelmann, E. & Lease, R. Late Miocene to Pleistocene Source to Sink Record
907 of Exhumation and Sediment Routing in the Gulf of Alaska from Detrital Zircon Fission-
908 Track and U-Pb Double Dating. *Tectonics* **38**, 2703–2726 (2019).
- 909 87. Huber, B., Bahlburg, H. & Pfänder, J. A. Single grain heavy mineral provenance of garnet
910 and amphibole in the Surveyor fan and precursor sediments on the Gulf of Alaska abyssal
911 plain — Implications for climate-tectonic interactions in the St. Elias orogen. *Sediment.*
912 *Geol.* **372**, 173–192 (2018).
- 913 88. Plafker, G., Moore, J. C., and Winkler, G. R. Geology of the southern Alaska margin. in
914 *The Geology of Alaska* (eds. Plafker, G. & Berg, H. C.) 389–448 (Geological Society of
915 America, 1994).
- 916 89. Harris, N. R., Sisson, V. B., Wright, J. E. & Pavlis, T. L. Evidence for Eocene mafic
917 underplating during fore-arc intrusive activity, eastern Chugach Mountains, Alaska.
918 *Geology* **24**, 263–266 (1996).
- 919 90. Sisson, V. B. *et al.* Geochemical and geochronologic constraints for genesis of a tonalite-
920 trondhjemite suite and associated mafic intrusive rocks in the eastern Chugach Mountains,
921 Alaska: A record of ridge-transform subduction. in *Geology of a transpressional orogen*
922 *developed during ridge-trench interaction along the North Pacific margin* (eds. Sisson, V.
923 B., Roeske, S. M. & Pavlis, T. L.) 293–326 (Geological Society of America, 2003).
- 924 91. Plafker, G., Nokleberg, W. J. & Lull, J. S. Bedrock geology and tectonic evolution of the
925 Wrangellia, Peninsular, and Chugach Terranes along the Trans-Alaska Crustal Transect in
926 the Chugach Mountains and Southern Copper River Basin, Alaska. *J. Geophys. Res. Solid*
927 *Earth* **94**, 4255–4295 (1989).
- 928 92. Polat, A. *et al.* Lithological, structural, and geochemical characteristics of the Mesoarchean
929 Tårtoq greenstone belt, southern West Greenland, and the Chugach – Prince William
930 accretionary complex, southern Alaska: evidence for uniformitarian plate-tectonic
931 processes. *Can. J. Earth Sci.* **53**, 1336–1371 (2016).
- 932 93. Lull, J. S., Plafker, G., Dover, J. H. & Galloway, J. P. Geochemistry and paleotectonic
933 implications of metabasaltic rocks in the Valdez Group, southern Alaska. *US Geol. Surv.*
934 *Bull.* **1946**, 29–38 (1990).
- 935 94. Barker, F., Farmer, G. L., Ayuso, R. A., Plafker, G. & Lull, J. S. The 50 Ma granodiorite of
936 the eastern Gulf of Alaska: Melting in an accretionary prism in the forearc. *J. Geophys. Res.*
937 *Solid Earth* **97**, 6757–6778 (1992).
- 938 95. Bruand, E., Gasser, D., Bonnand, P. & Stuewe, K. The petrology and geochemistry of a
939 metabasite belt along the southern margin of Alaska. *Lithos* **127**, 282–297 (2011).
- 940 96. Walinsky, S. E. *et al.* Distribution and composition of organic matter in surface sediments
941 of coastal Southeast Alaska. *Cont. Shelf Res.* **29**, 1565–1579 (2009).
- 942 97. Haskell, K. H. & Hanson, R. J. An algorithm for linear least squares problems with equality
943 and nonnegativity constraints. *Math. Program.* **21**, 98–118 (1981).
- 944 98. Bolton, M. S. M. *et al.* Machine learning classifiers for attributing tephra to source
945 volcanoes: an evaluation of methods for Alaska tephtras. *J. Quat. Sci.* **35**, 81–92 (2020).
- 946 99. Bryson, R. U., Bryson, R. A. & Ruter, A. A calibrated radiocarbon database of late
947 Quaternary volcanic eruptions. *EEarth Discuss* **1**, 123–134 (2006).
- 948 100. Watt, S. F. L., Pyle, D. M. & Mather, T. A. The volcanic response to deglaciation:
949 Evidence from glaciated arcs and a reassessment of global eruption records. *Earth-Sci. Rev.*
950 **122**, 77–102 (2013).

- 951 101. Crossweller, H. S. *et al.* Global database on large magnitude explosive volcanic eruptions
952 (LaMEVE). *J. Appl. Volcanol.* **1**, 4 (2012).
- 953 102. Davies, L. J., Jensen, B. J. L., Froese, D. G. & Wallace, K. L. Late Pleistocene and
954 Holocene tephrostratigraphy of interior Alaska and Yukon: Key beds and chronologies over
955 the past 30,000 years. *Quat. Sci. Rev.* **146**, 28–53 (2016).
- 956 103. Reimer, P. J. *et al.* The IntCal20 Northern Hemisphere Radiocarbon Age Calibration Curve
957 (0–55 cal kBP). *Radiocarbon* **62**, 725–757 (2020).
- 958 104. Kalnay, E. *et al.* The NCEP/NCAR 40-Year Reanalysis Project. *Bull. Am. Meteorol. Soc.*
959 **77**, 437–472 (1996).
- 960 105. Lesnek, A. J., Briner, J. P., Baichtal, J. F. & Lyles, A. S. New constraints on the last
961 deglaciation of the Cordilleran Ice Sheet in coastal Southeast Alaska. *Quat. Res.* **96**, 140–
962 160 (2020).
- 963 106. Haeussler, P. J. *et al.* Late Quaternary deglaciation of Prince William Sound, Alaska. *Quat.*
964 *Res.* **105**. 115–135 (2022).
- 965 107. Walcott, C. K., Briner, J. P., Baichtal, J. F., Lesnek, A. J. & Licciardi, J. M. Cosmogenic
966 ages indicate no MIS 2 refugia in the Alexander Archipelago, Alaska. *Geochronology* **4**,
967 191–211 (2022).
- 968 108. Briner, J. P. *et al.* The last deglaciation of Alaska. *Cuad. Investig. Geográfica* **43**, 429–448
969 (2017).
- 970 109. Tulenko, J. P., Briner, J. P., Young, N. E. & Schaefer, J. M. Beryllium-10 chronology of
971 early and late Wisconsinan moraines in the Revelation Mountains, Alaska: Insights into the
972 forcing of Wisconsinan glaciation in Beringia. *Quat. Sci. Rev.* **197**, 129–141 (2018).
- 973 110. Menounos, B. *et al.* Cordilleran Ice Sheet mass loss preceded climate reversals near the
974 Pleistocene Termination. *Science* **358**, 781–784 (2017).
- 975 111. Dulfer, H. E., Margold, M., Engel, Z., Braucher, R. & Team, A. Using ¹⁰Be dating to
976 determine when the Cordilleran Ice Sheet stopped flowing over the Canadian Rocky
977 Mountains. *Quat. Res.* **102**, 222–233 (2021).
- 978 112. R Core Team. R: A language and environment for statistical computing. (2013).
- 979 113. Seguinot, J. *et al.* Cordilleran ice sheet glacial cycle simulations continuous variables [Data
980 set]. Zenodo. <https://doi.org/10.5281/zenodo.3606536> (2020).
- 981 114. Dansgaard, W. *et al.* Evidence for general instability of past climate from a 250-kyr ice-
982 core record. *Nature* **364**, 218–220 (1993).
- 983 115. Andersen, K. K. *et al.* High-resolution record of Northern Hemisphere climate extending
984 into the last interglacial period. *Nature* **431**, 147–151 (2004).
- 985 116. Jouzel, J. *et al.* Orbital and Millennial Antarctic Climate Variability over the Past 800,000
986 Years. *Science* **317**, 793–796 (2007).
- 987 117. Petit, J. R. *et al.* Climate and atmospheric history of the past 420,000 years from the Vostok
988 ice core, Antarctica. *Nature* **399**, 429–436 (1999).
- 989 118. Herbert, T. D. *et al.* Collapse of the California Current During Glacial Maxima Linked to
990 Climate Change on Land. *Science* **293**, 71–76 (2001).
- 991 119. Behrenfeld, M. J. & Falkowski, P. G. Photosynthetic rates derived from satellite-based
992 chlorophyll concentration. *Limnol. Oceanogr.* **42**, 1–20 (1997).
- 993 120. Roberts, M. V. The temporal and spatial distribution of dissolved and particulate iron over
994 the Gulf of Alaska shelf. (University of Alaska Fairbanks, 2018).
- 995 121. Tagliabue, A. *et al.* A global compilation of dissolved iron measurements: focus on
996 distributions and processes in the Southern Ocean. *Biogeosciences* **9**, 2333–2349 (2012).

- 997 122. GEOTRACES Intermediate Data Product Group. The GEOTRACES Intermediate Data
998 Product 2021 (IDP2021). NERC EDS British Oceanographic Data Centre NOC.
999 [https://www.bodc.ac.uk/data/published_data_library/catalogue/10.5285/cf2d9ba9-d51d-
1000 3b7c-e053-8486abc0f5fd/](https://www.bodc.ac.uk/data/published_data_library/catalogue/10.5285/cf2d9ba9-d51d-3b7c-e053-8486abc0f5fd/) (2021).
- 1001 123. Hauri, C. *et al.* A regional hindcast model simulating ecosystem dynamics, inorganic
1002 carbon chemistry, and ocean acidification in the Gulf of Alaska. *Biogeosciences* **17**, 3837–
1003 3857 (2020).
- 1004 124. Garcia, H. *et al.* World Ocean Atlas 2018. Vol. 4: Dissolved Inorganic Nutrients
1005 (phosphate, nitrate and nitrate+nitrite, silicate). A. Mishonov Technical Editor, NOAA
1006 Atlas NESDIS 84, 35pp. (2019).
- 1007 125. Zweng, M. *et al.* World Ocean Atlas 2018, Volume 2: Salinity. A. Mishonov, Technical
1008 Editor, NOAA Atlas NESDIS 82, 50pp. (2019).
- 1009 126. Le Maitre, R. W. *et al.* *Igneous Rocks: A Classification and Glossary of Terms:
1010 Recommendations of the International Union of Geological Sciences Subcommission on the
1011 Systematics of Igneous Rocks.* (Cambridge University Press, 2002).
- 1012 127. McDonough, W. F. & Sun, S. -s. The composition of the Earth. *Chem. Geol.* **120**, 223–253
1013 (1995).
1014

1015 **Acknowledgements**

1016 We thank Jesse Muratli for assistance in geochemical analysis at OSU. Funding for this study
1017 was provided by US NSF Award 1502754 to A.C.M. and 1801511 to C.L.B. J.D. was supported
1018 by the ETH Zurich Postdoctoral Fellowship 19-2 FEL-32. This project has received funding
1019 from the European Union’s Horizon 2020 research and innovation programme under the Marie
1020 Skłodowska-Curie grant agreement 891489. We thank the Oregon State University Marine and
1021 Geology Repository and the International Ocean Discovery Program for access to core materials.

1022 **Author contributions**

1023 J.D. and A.C.M designed this study. J.D. conducted the geochemical analysis and modelling,
1024 data compilation and synthesis, and led the writing of the manuscript. A.C.M. assisted the overall
1025 conceptualisation and interpretation of results and contributed significantly to the writing of the
1026 manuscript. B.A.H assisted with the interpretation of geochemical data and writing of the
1027 manuscript. C.L.B and Sharon helped with the faunal-trace metal data comparison and analysis.

1028 **Competing interests**

1029 The authors declare no competing interests.

1030 **Additional information**

1031 **Correspondence and requests for materials** should be addressed to Jianghui Du
1032 (jianghui.du@erdw.ethz.ch).

1033 **Reprints and permissions information** is available at www.nature.com/reprints.

1034

1035 **Extended Data Legends**

1036 **Extended Data Figure 1 | Modern biogeochemistry of the Gulf of Alaska. a**, Net primary
1037 production, based on the Vertically Generalised Production Model and the Moderate Resolution
1038 Imaging Spectroradiometer satellite results¹¹⁹, and integrated over the euphotic zone and
1039 averaged over the spring and summer months (April to September) from 2002 to 2020. **b**,
1040 Surface water dissolved Fe concentrations, measured^{52–54,120–122} (triangle symbols, averaged over
1041 0–100 m) and from a high resolution regional hind-cast model¹²³ (background colour, averaged
1042 over 0–100 m and the spring and summer months from 1980 to 2013). The colour bar is in log
1043 scale. **c**, Surface NO₃⁻ climatology (μM, 1 degree grid) from the World Ocean Atlas (WOA)
1044 2018¹²⁴, averaged over 0–100 m and the spring and summer months. **d**, Surface salinity
1045 climatology (0.25 degree grid) from the WOA 2018¹²⁵, at 0 m and averaged over the summer
1046 months. The three black lines in **a–c** are the isobaths of 300 m, indicating the depth of the shelf
1047 break; 680 m, the depth of site 85JC/U1419; and 3680 m, the depth of site 87JC/U1418. The
1048 three black lines in **d** are the isohalines of 30, 31 and 32. The white arrow in **d** indicates the
1049 Alaska Coastal Current (ACC).

1050

1051 **Extended Data Figure 2 | Bchron⁶¹ Bayesian age models. a–f**, Age model construction for the
1052 intermediate-depth site^{4,17}. **a**, Radiocarbon dates (points) calibrated using the Marine20 curve²¹
1053 and the modelled depth-age relationship (median line with 1σ range). **b**, Sedimentation rate
1054 (median line with 1σ range). **c**, The depth conversion used to align 85JC to U1419. **d**, The
1055 normalised and weighted RMSE of GRA and MS misfits as a function of the deviation from the
1056 depth conversion in **c**. **e**, Aligned magnetic susceptibility records. **f**, Aligned GRA density
1057 records. **g–k**, Age model construction for the abyssal site²⁰. Only MS was used for alignment in
1058 this case. **g**, Radiocarbon dates (points) calibrated using the Marine20 curve²¹ and the modelled
1059 depth-age relationship (median line with 1σ range). **h**, Sedimentation rate (median line with 1σ

1060 range). **i**, The depth conversion used to align 87JC to U1418. **j**, The normalised RMSE of MS
1061 misfit as a function of the deviation from the depth conversion in **i**. **k**, Aligned magnetic
1062 susceptibility records.

1063

1064 **Extended Data Figure 3 | Geochemistry of the volcanic endmembers identified by cluster**
1065 **analysis. a**, Total Alkali Silica (TAS) diagram¹²⁶. Each point represents a sample and the 1σ
1066 confidence ellipses of the clusters are shown. **b**, Chondrite¹²⁷ normalised REE patterns. **c**,
1067 Primitive mantle¹²⁷ normalised trace element patterns. The shaded intervals indicate the 1σ
1068 ranges (geometric mean and standard deviation) of the endmembers. **d**, Locations of volcanic
1069 samples. Unfilled circles indicate lava (whole rock) samples. Filled circles indicate tephra
1070 (volcanic glass) samples. The locations of the tephra samples are the locations where they were
1071 deposited.

1072

1073 **Extended Data Figure 4 | Geochemistry of the potential terrigenous sediment endmembers**
1074 **compared with sediments at the intermediate-depth site. a-c**, Bi-element plots showing the
1075 relationships between GOA Holocene and LGM (H&L) sediments and the terrigenous
1076 endmembers⁸⁹⁻⁹⁵. **d**, Aitchison distances among the GOA Holocene and LGM sediments, and
1077 between them and the terrigenous endmembers⁸⁹⁻⁹⁵. Distances are calculated for all possible
1078 sample pairs. The y-axis is sorted in the order of increasing median distance. The results are
1079 summarised using violin plots. The first row in **d** indicates the internal differences among the
1080 GOA Holocene and LGM samples, while the other rows indicate external differences between
1081 the GOA samples and terrigenous endmembers.

1082

1083 **Extended Data Figure 5 | Geochemical data inversion at the intermediate-depth site. a**,
1084 Weight fractions of the volcanic endmembers, and the terrigenous fractions. **b**, Total volcanic
1085 fraction versus total sediment MAR⁴. Lines and shaded intervals (95% CI) indicate linear
1086 regression ($p > 0.5$). **c**, Box plots of weighted residuals of the elements in the solution of the
1087 geochemical inverse problem. Boxes indicate the interquartile range (IQR); thick lines indicate
1088 the medians; whiskers extend to 1.5 IQR away from the boxes.

1089

1090 **Extended Data Figure 6 | Records of volcanism since the LGM compiled by this study**
1091 **compared with that of ref⁵ (HL09).** **a**, Eruption frequencies of volcanoes binned at 2-kyr
1092 intervals. For glaciated volcanoes, the total frequency, as well as the frequency of regional
1093 glaciated volcanoes from the Northeast Pacific margin and the rest of the world are shown. **b**,
1094 The ratios of the eruption frequency of the glaciated volcanoes (global total, from the Northeast
1095 Pacific margin, or elsewhere) to that of the global unglaciated volcanoes, normalised to the mean
1096 ratios during the LGM, used as proxies for glacially induced volcanism. The ribbons indicate
1097 interquartile ranges. The eruption frequency ratio increases between 12 and 6 ka in HL09, much
1098 later than our new compilation (17–11 ka). However, this is because the eruptions of unglaciated
1099 volcanoes were under-sampled in HL09 during the deglaciation because their database was
1100 smaller (**a**). With greater data coverage, this issue of under-sampling appears resolved in our new
1101 compilation.

1102

1103 **Extended Data Figure 7 | Northeast Pacific productivity proxies.** **a**, CaCO₃ content^{19,28}. **b**,
1104 Sediment Sr/Al ratio. **c**, Counts of coccolith per field of view (FoV)¹⁹. **d**, TOC content²⁸. **e**, Opal
1105 content²⁸. **f**, Bulk sediment $\delta^{15}\text{N}$, corrected for terrestrial organic matter input²⁸. **g**, Sediment
1106 Ba/Al ratio. The y-axis scales are different between the intermediate-depth and abyssal sites. **h**,
1107 Abundances of productivity-related benthic foraminifera species *Islandiella norcrossi* from the
1108 intermediate-depth site and *Elphidium batialis* from the abyssal site^{12,23}. The colour legends in **a**–
1109 **h** are the same.

1110

1111 **Extended Data Figure 8 | Records of Northeast Pacific deoxygenation compared with other**
1112 **regional and global climate proxies.** **a**, Re/Al ratios from the GOA sites. **b**, Benthic-planktonic
1113 radiocarbon age difference (with 1 σ uncertainty) at the intermediate-depth site^{4,17}, a proxy for
1114 intermediate water ventilation. **c**, $\delta^{18}\text{O}$ (with 1 σ uncertainty) of surface seawater in the Northeast
1115 Pacific after removing global ice volume effect²⁹, a proxy for surface salinity. **d**, Relative sea
1116 level in the northern GOA³¹ (points with smoothed lines and 95% CI). **e**, ²³¹Pa/²³⁰Th (with 1 σ
1117 uncertainty) from the North Atlantic³², a proxy for the overturning strength of AMOC. **e**,

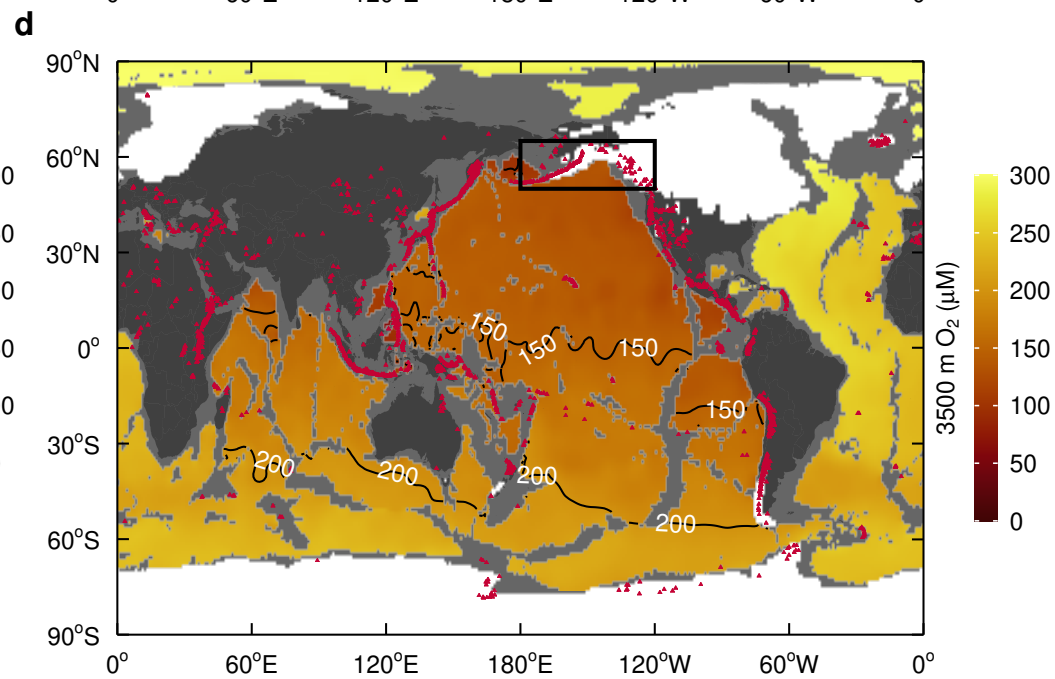
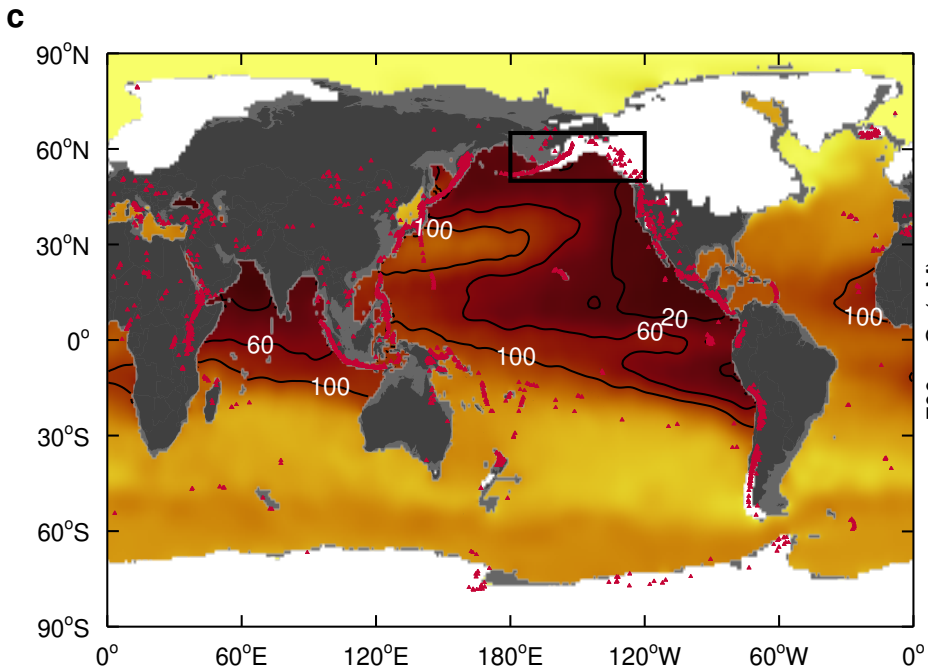
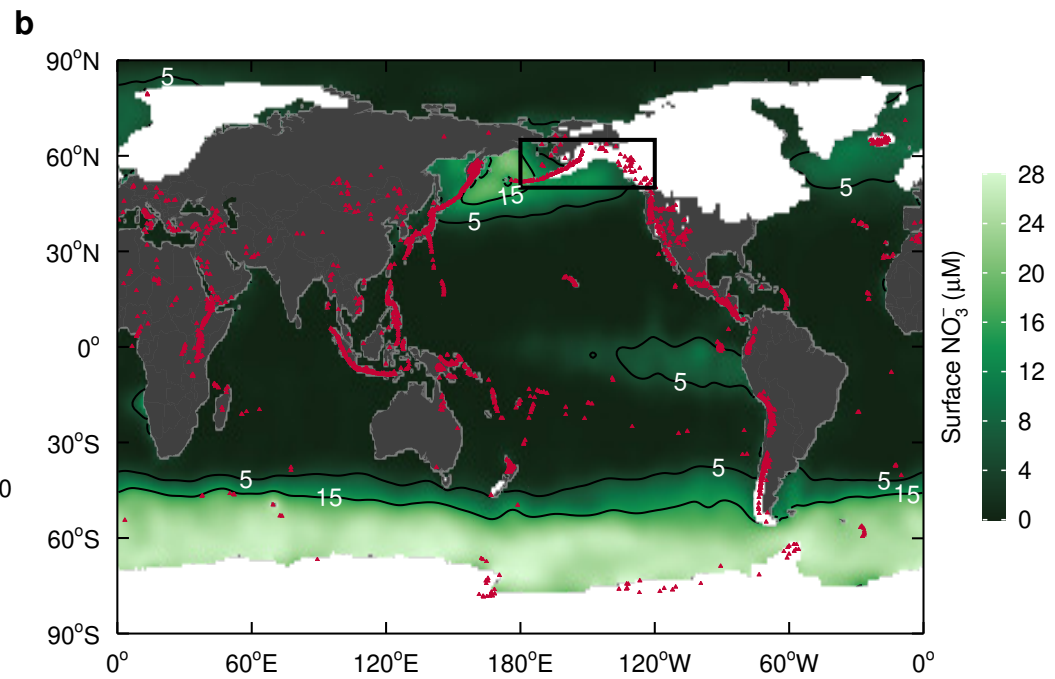
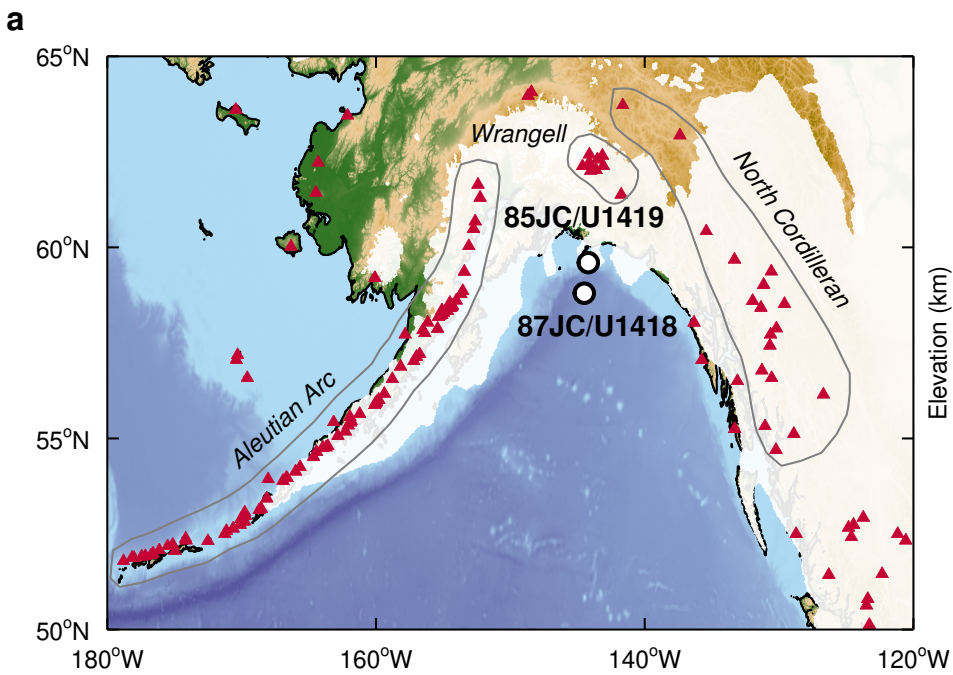
1118 Terrestrial ^4He flux (with 1σ uncertainty) from the subpolar North Pacific³³, a proxy for mineral
1119 dust flux that is *not* affected by volcanic ash input.

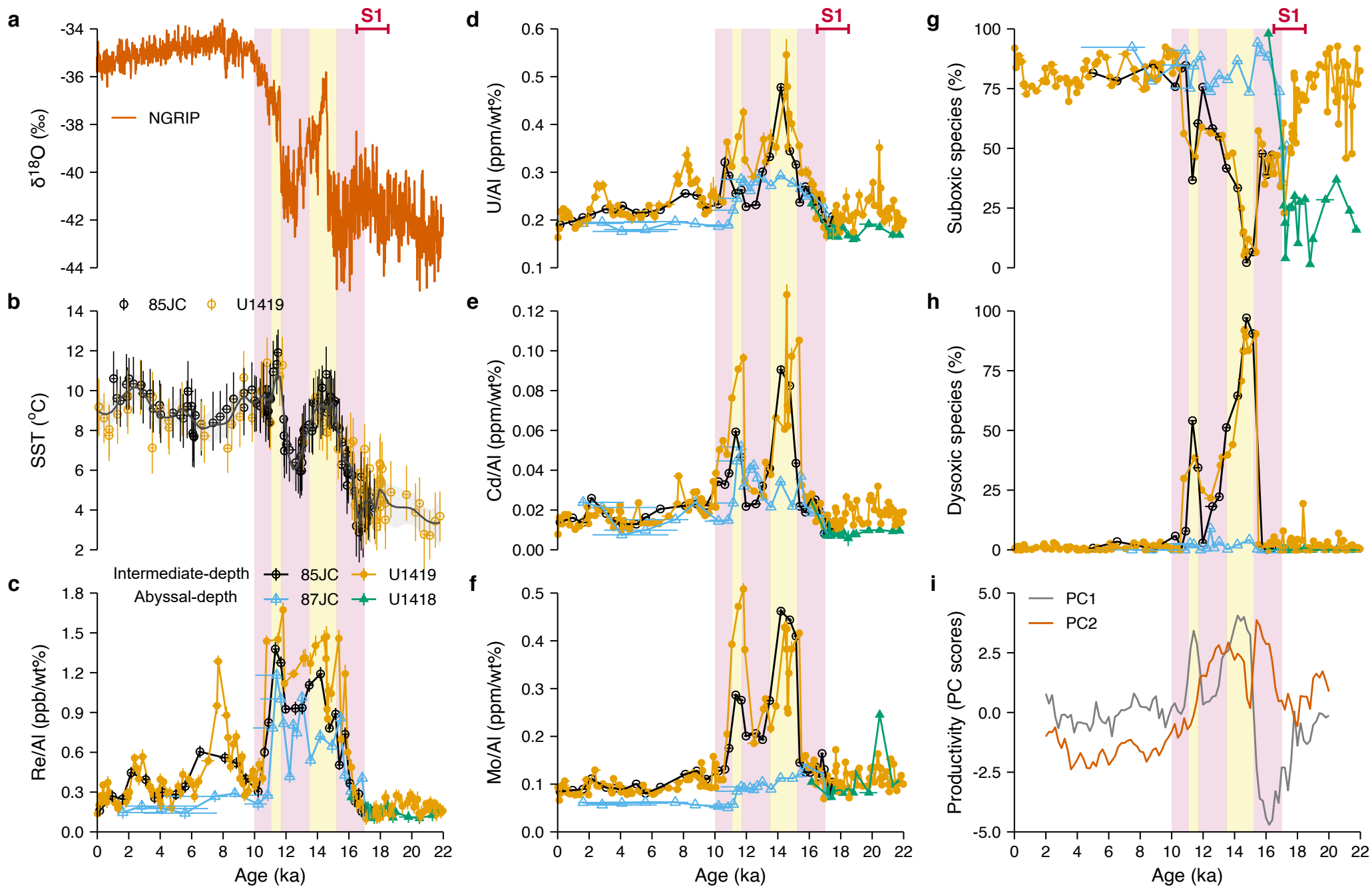
1120

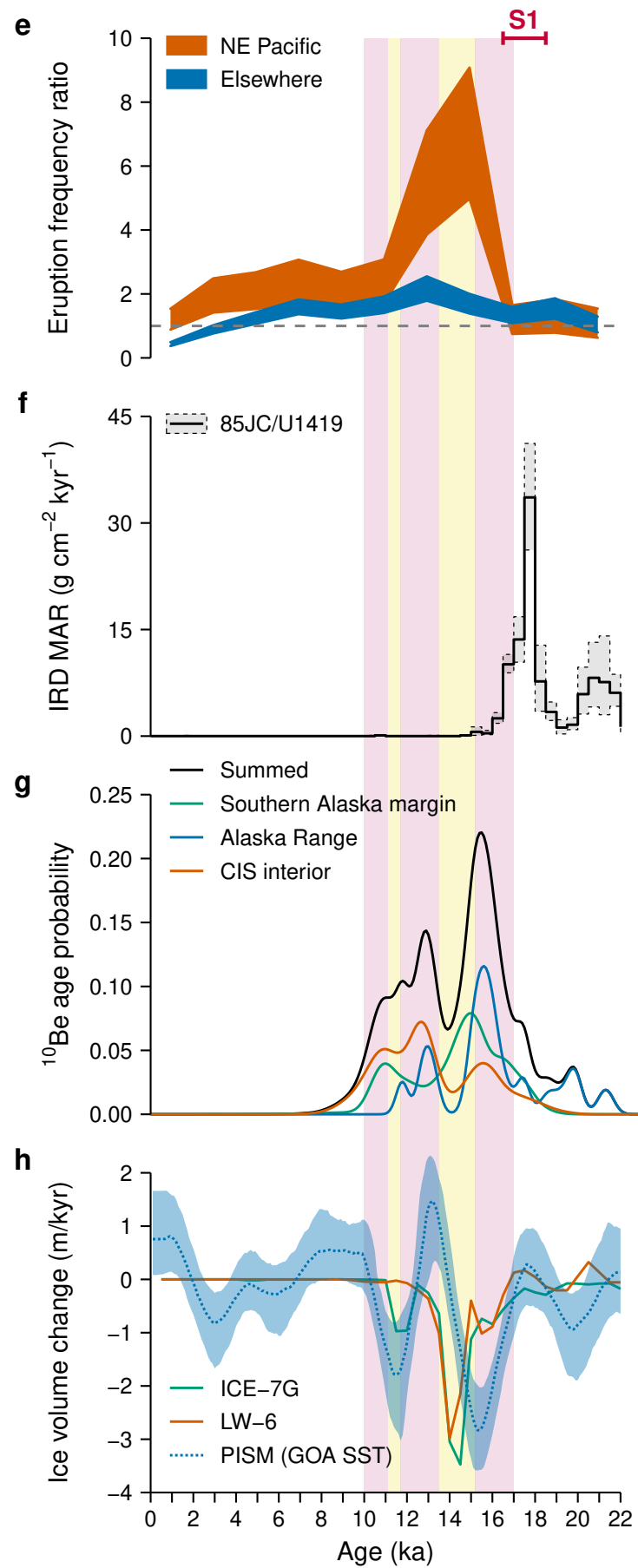
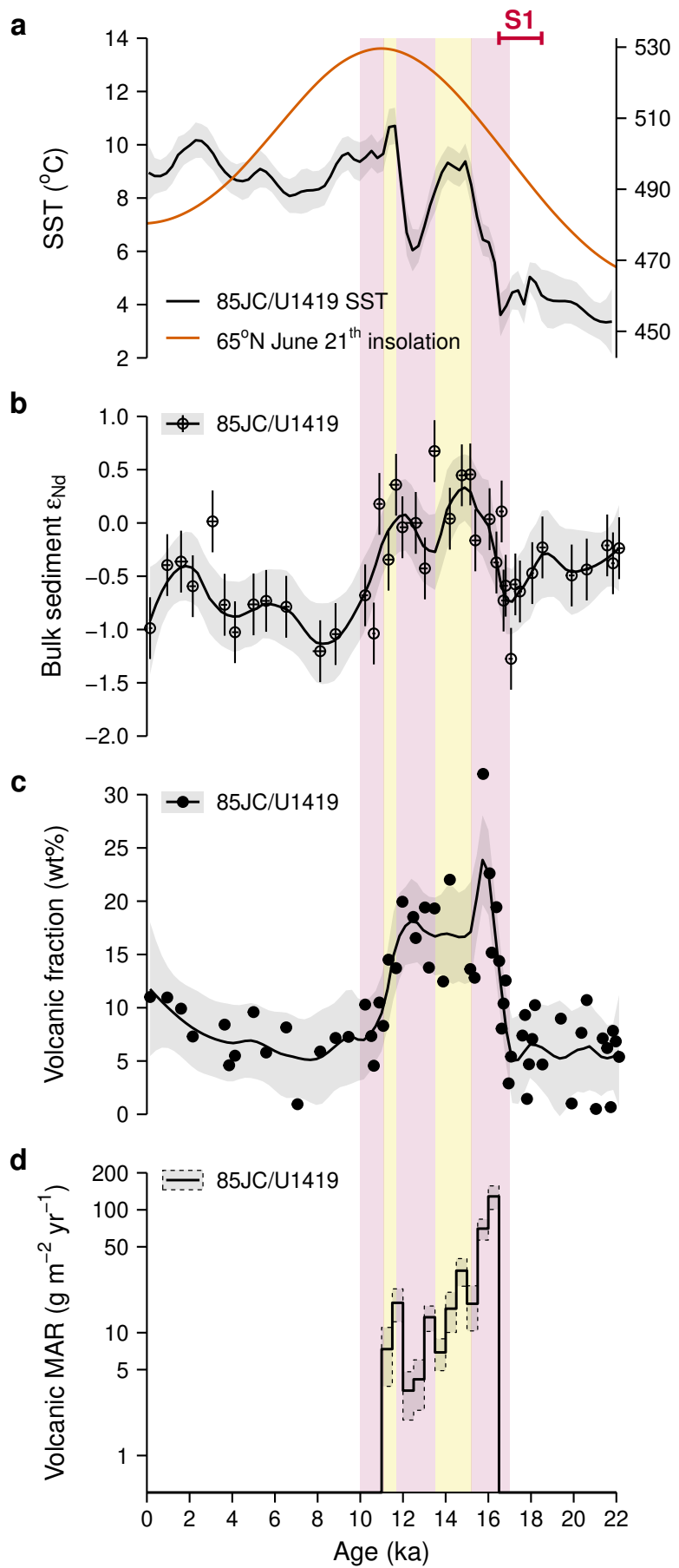
1121 **Extended Data Figure 9 | Histories of the Cordilleran Ice Sheet. a**, Radiocarbon based ice
1122 sheet extent reconstruction from 20 ka to 12 ka⁴¹. **b**, Changes of ice thickness in the ICE-7G
1123 model from 20 ka to 12 ka²⁵. Red colour indicates ice loss while blue colour indicates ice
1124 accumulation.

1125

1126 **Extended Data Figure 10 | Sensitivity of the Cordilleran Ice Sheet volume to the surface**
1127 **temperature forcing in the PISM model**²⁷. **a**, Temperature forcing used in the sensitivity
1128 experiments (relative to the modern mean) derived from the following temperature records:
1129 EPICA¹¹⁶, GRIP¹¹⁴, NGRIP¹¹⁵, VOSTOK¹¹⁷, ODP 1012 and 1020¹¹⁸. **b**, Modelled CIS volume in
1130 terms of sea-level equivalent. In the EPICA and GRIP experiments both 5 km and 10 km spatial
1131 resolutions were used, while in other experiments only 10 km resolution was used²⁷. **c**, Rate of
1132 CIS volume change (500-year binned averages). **d**, Lead-lag between the ice volume response
1133 and the temperature forcing. Estimated time-lags are indicated by the vertical lines according to
1134 the highest negative cross-correlation, and the results are shown in the legends inside brackets. **e**,
1135 Sensitivity of CIS volume to the temperature forcing. Linear regression (lines with 95% CI, r^2
1136 between 0.82 and 0.94, $p \ll 0.05$) were performed after shifting the temperature forcing by the
1137 time-lags estimated in **c**. Estimated sensitivities in metre sea-level equivalent/ $^{\circ}\text{C}$ are shown in the
1138 legends inside brackets. **f**, Predicted rates of CIS volume change (median values) if the GOA
1139 SST record is used as the temperature forcing. The results were estimated using the ice volume-
1140 temperature relationship in each sensitivity experiments. The final estimate in Fig. 3h
1141 incorporates all the sensitivity experiments and uncertainties.

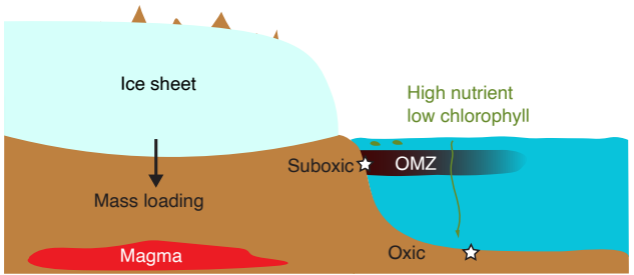






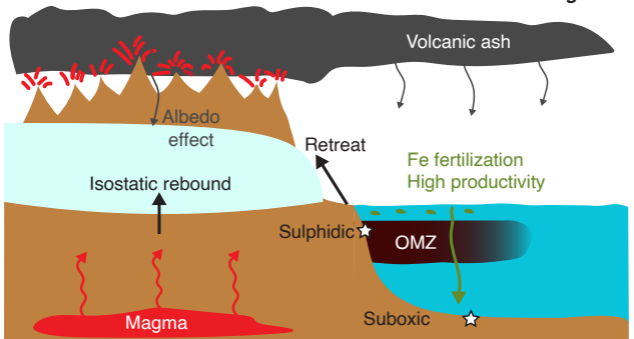
Glacial

a



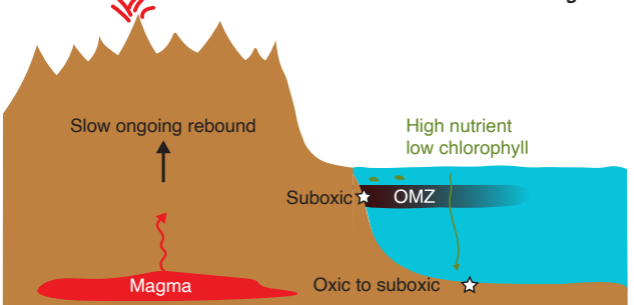
Deglacial

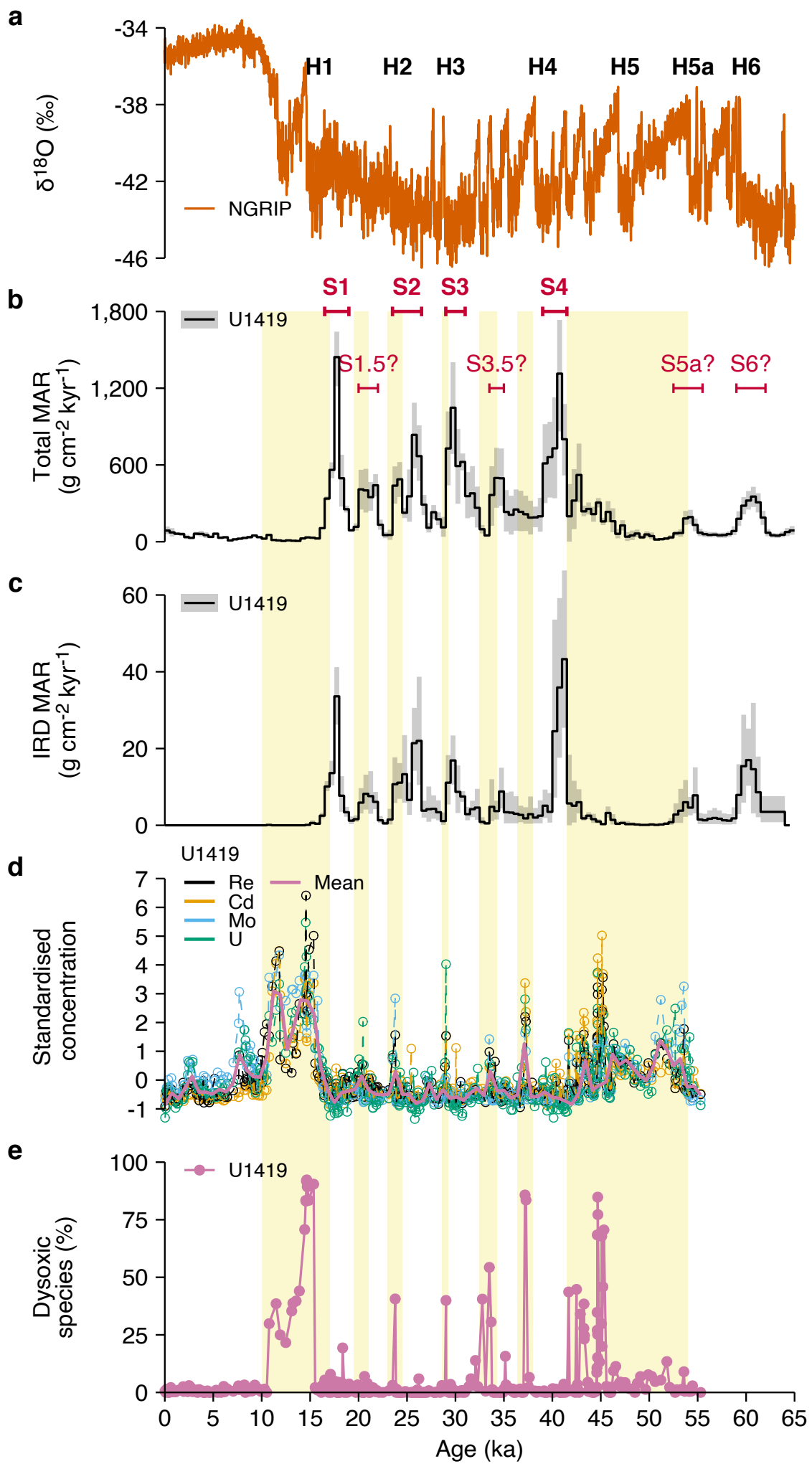
b

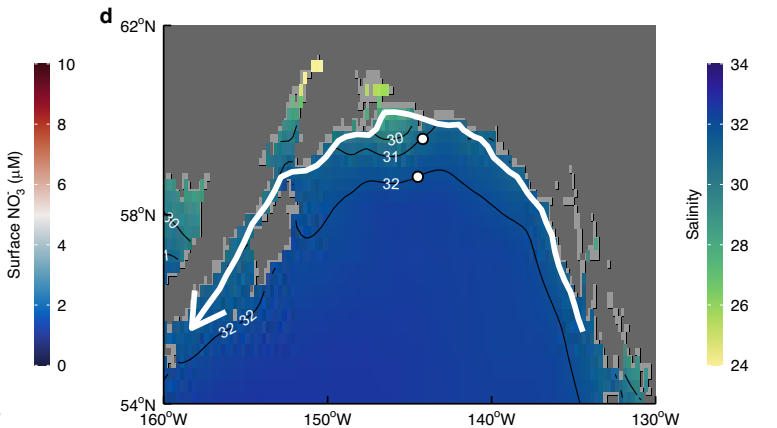
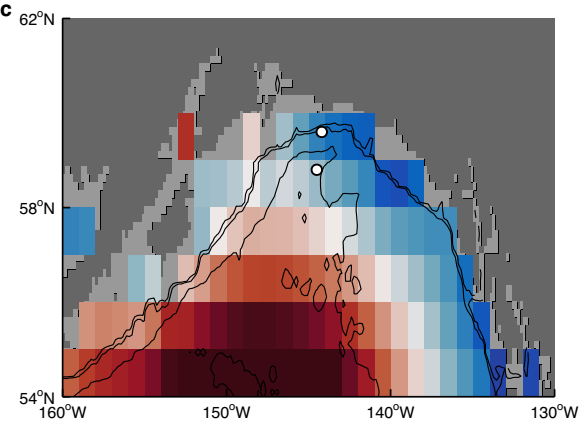
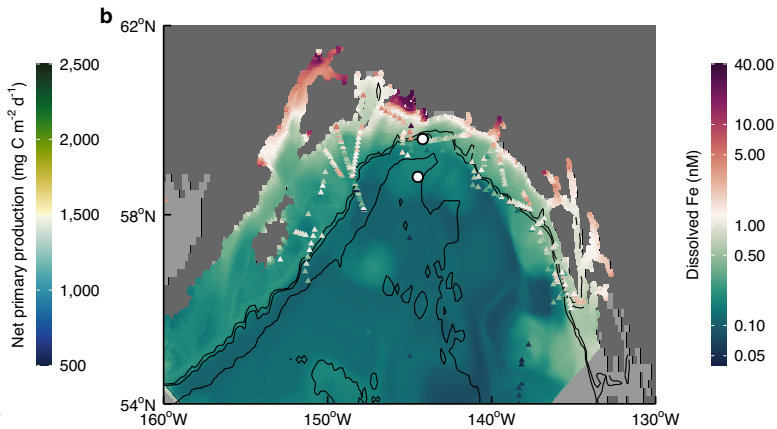
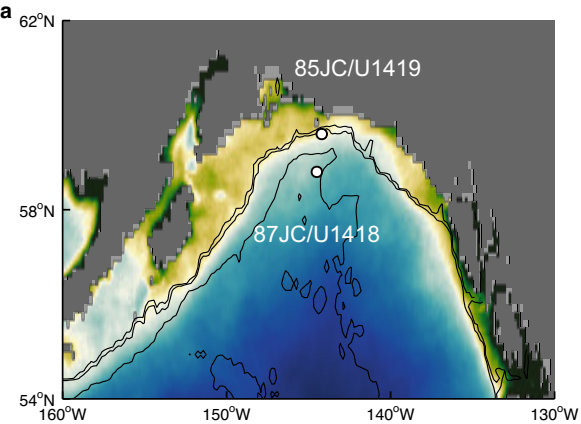


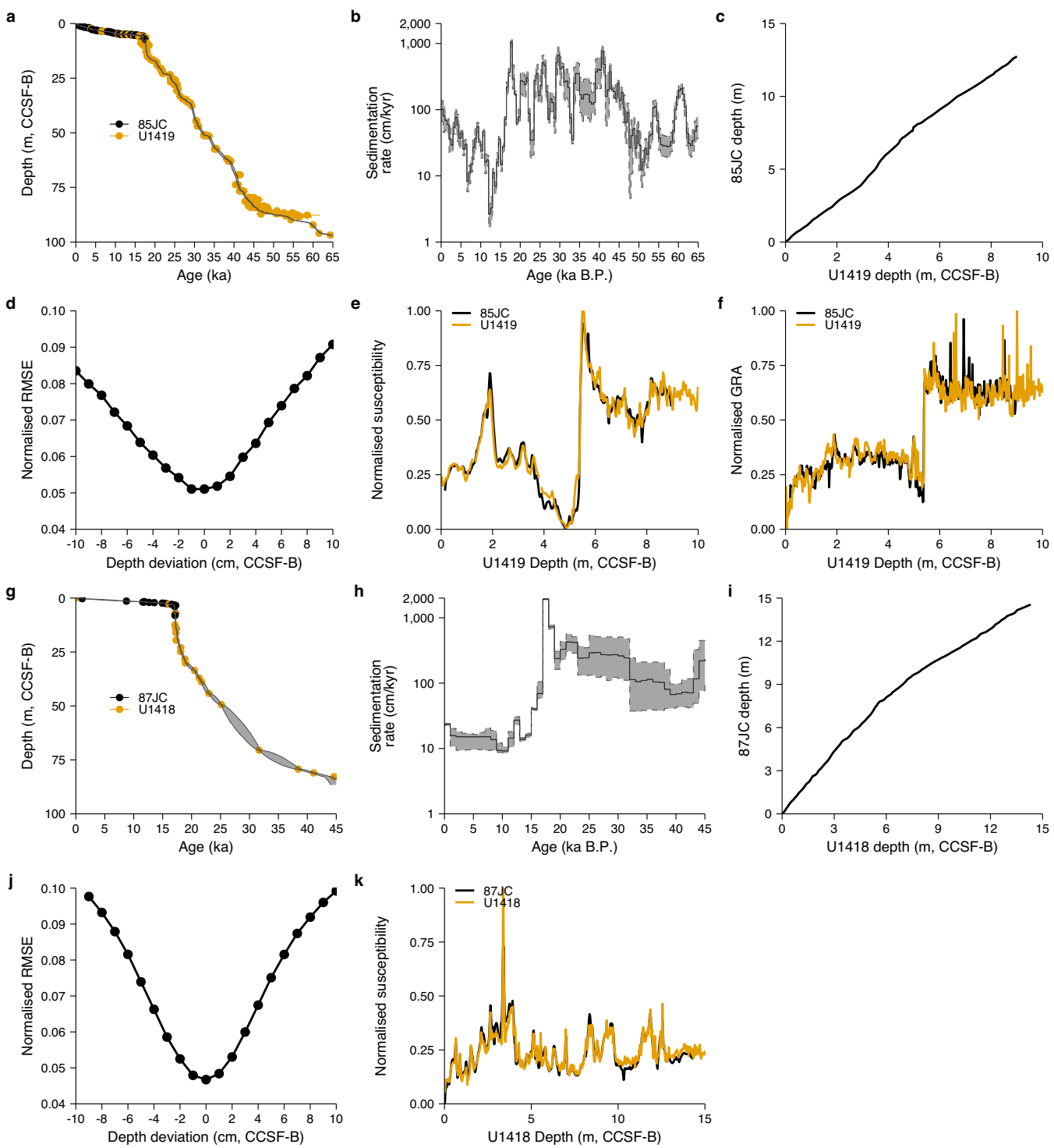
Interglacial

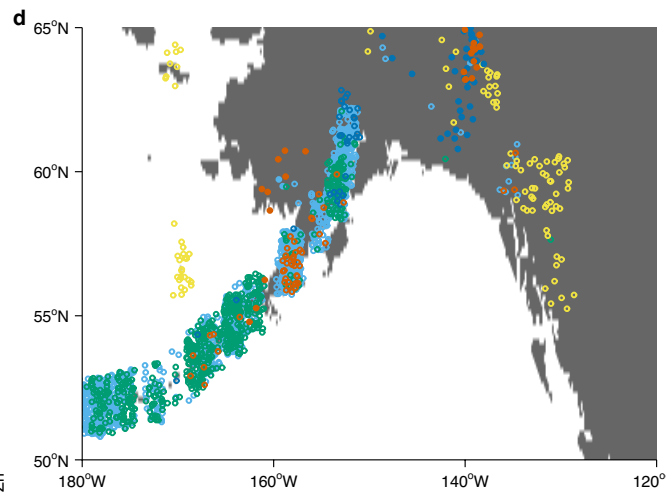
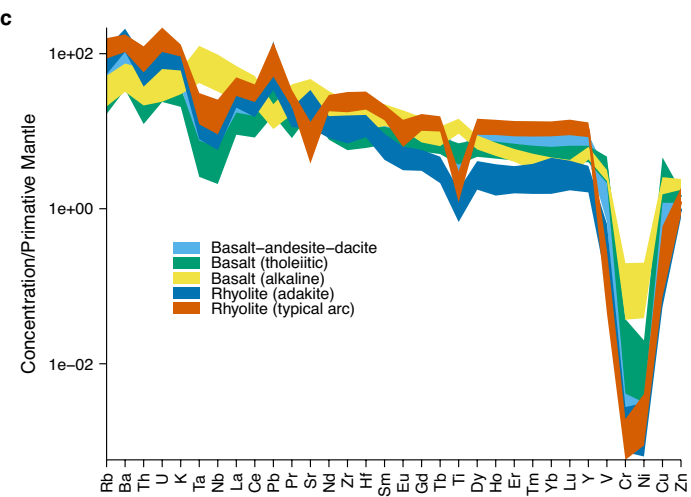
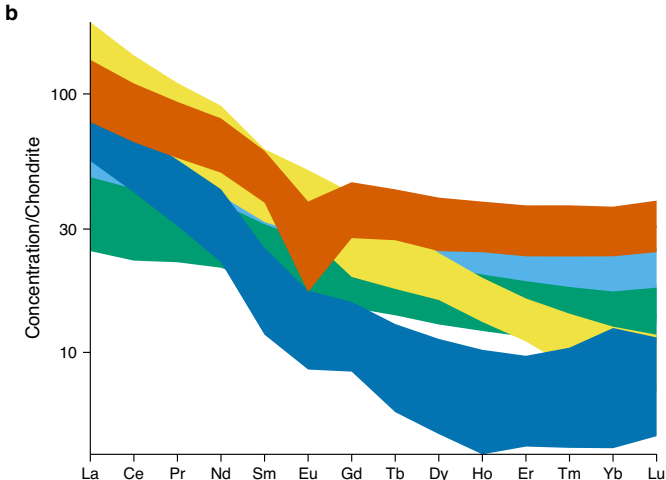
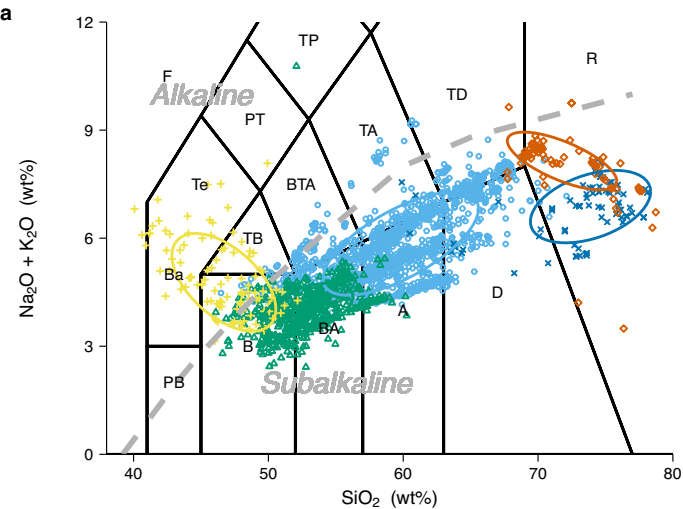
c

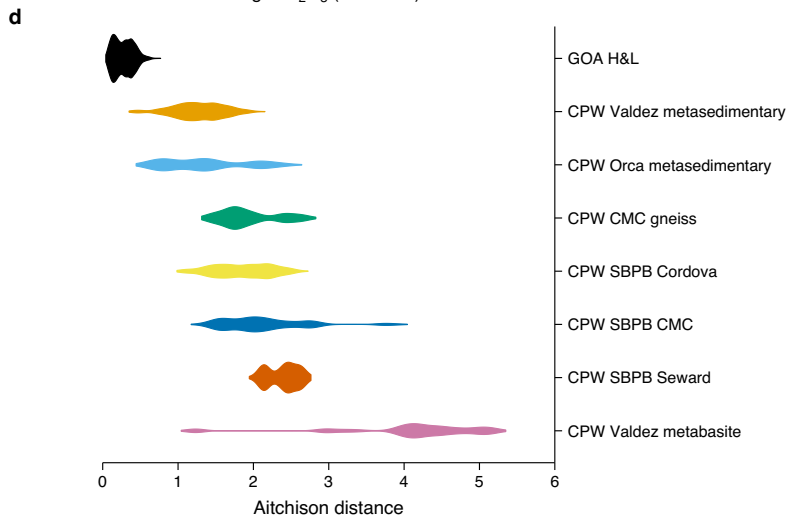
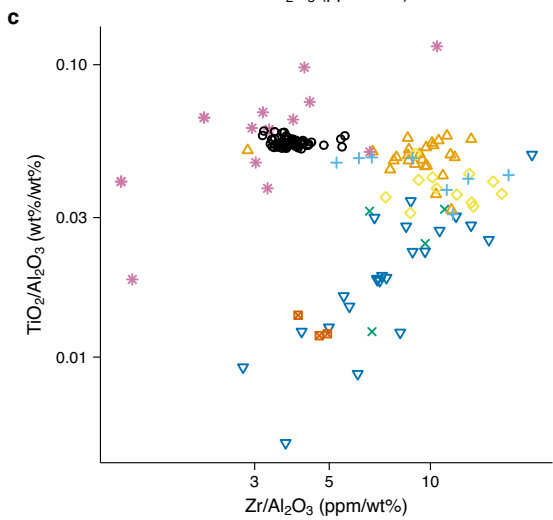
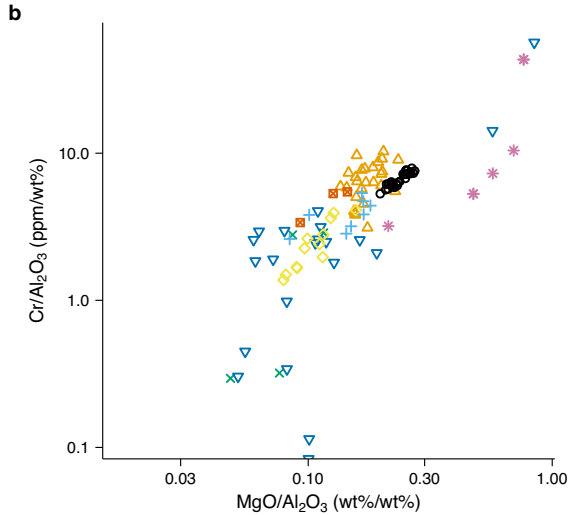
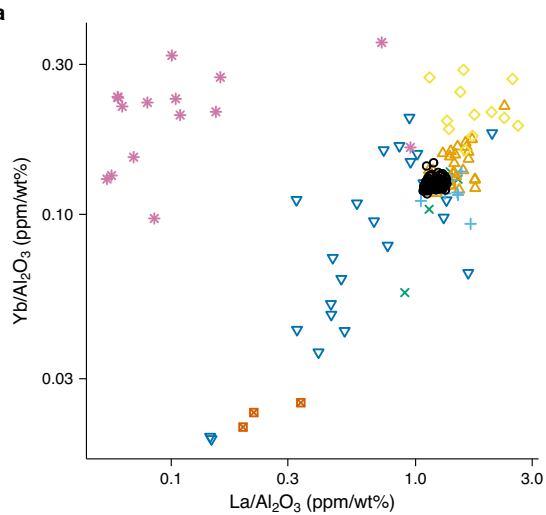


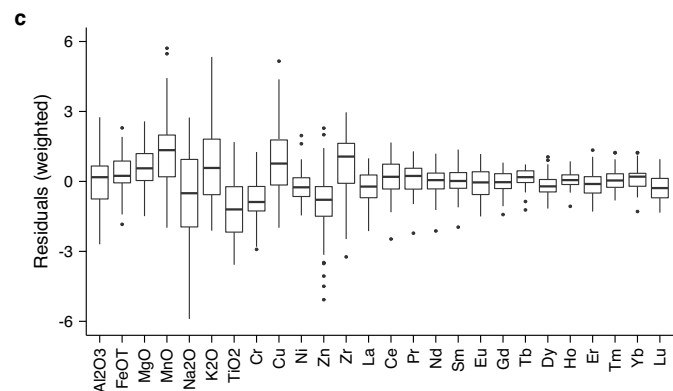
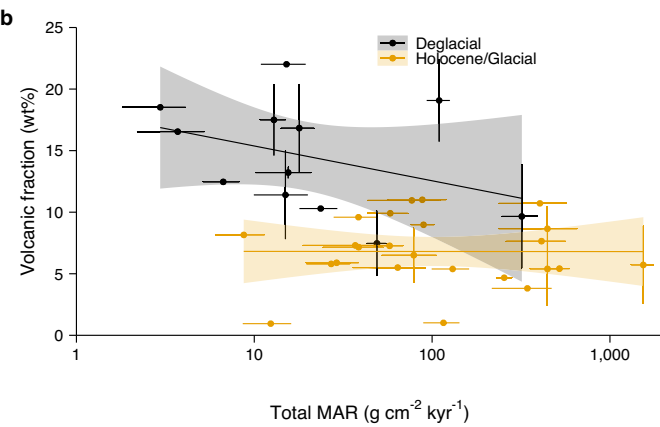
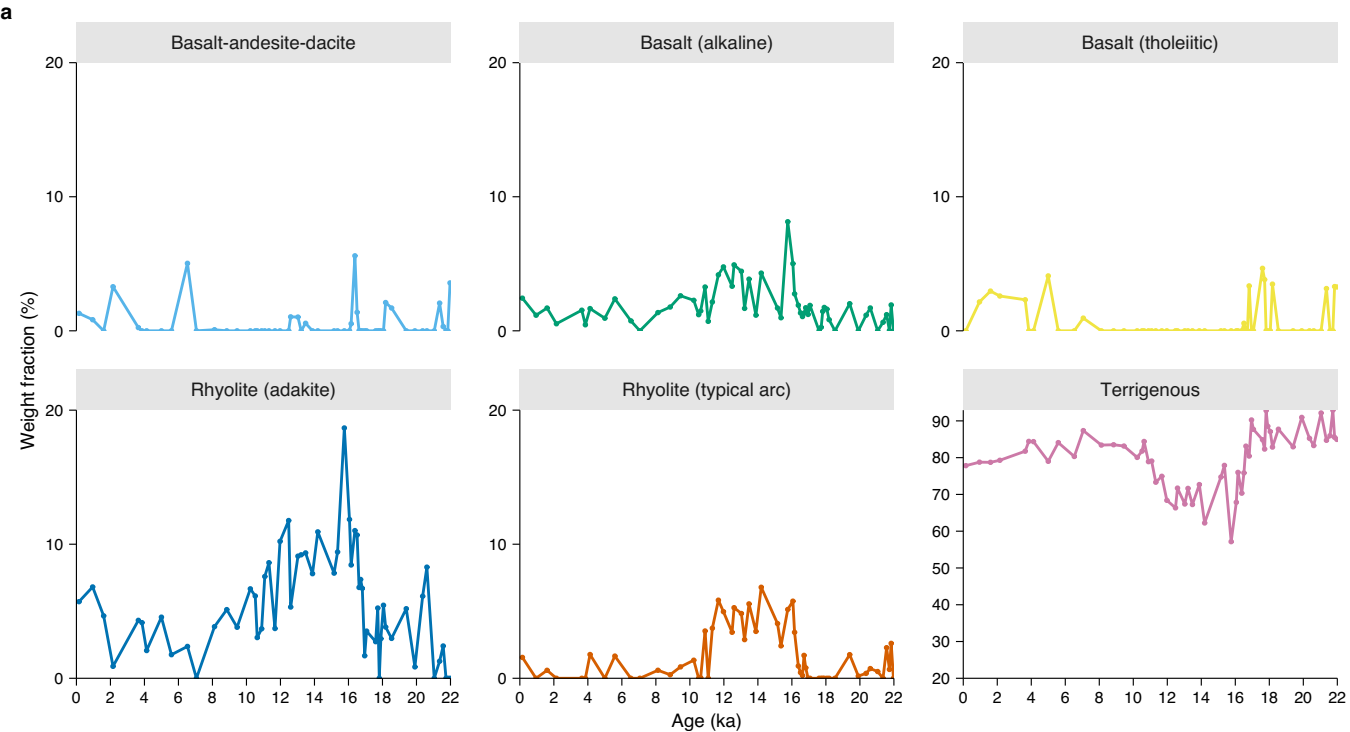


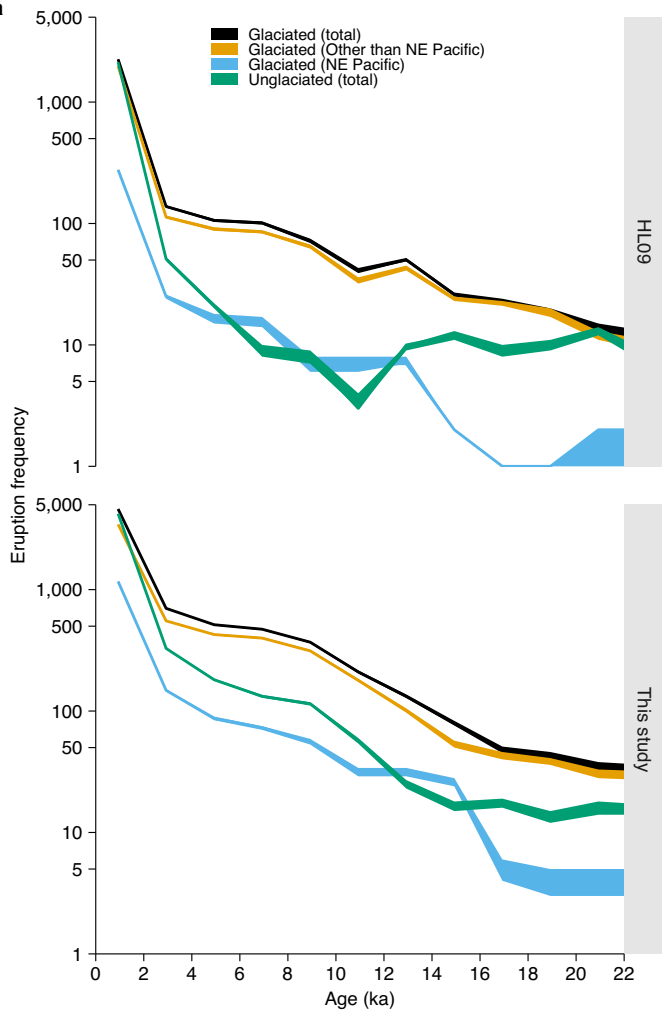










a**b**